



Ψ_k Scientific Highlight of the Month

No. 139

February 2018

Magnetic skyrmions: structure, stability, and transport phenomena

G. Bihlmayer^{1,†}, P. M. Buhl¹, B. Dupé^{1,2}, I. L. Fernandes¹, F. Freimuth¹, J. Gayles^{1,3},
S. Heinze⁴, N. Kiselev¹, S. Lounis¹, Y. Mokrousov¹, and S. Blügel¹

¹ *Peter Grünberg Institut and Institute for Advanced Simulation, Forschungszentrum Jülich
and JARA, D-52425 Jülich Germany*

² *Institute of Physics, Johannes Gutenberg Universität Mainz, 55128 Mainz, Germany*

³ *Max Planck Institute for Chemical Physics of Solids, 01187 Dresden, Germany*

⁴ *Institute of Theoretical Physics and Astrophysics, University of Kiel, 24098 Kiel, Germany*

Abstract

Magnetic skyrmions in chiral magnets are two-dimensionally localized and topologically protected vortex-like magnetic textures with particle-like properties. They are currently under intense scrutiny as an entity enabling new and exciting concepts in information storage and processing within the framework of spintronics. Their stability results from the Dzyaloshinskii-Moriya interaction, which originates from the spin-orbit interaction in magnets lacking bulk or structure inversion symmetry. The skyrmions are exciting not only due to their stability but also due to the presence of a quantized topological charge, a quantized topological orbital moment, emergent electrodynamics, a topological Hall effect, non-reciprocal excitations, non-collinear magnetic textures characterized by scalar and vector spin-chiralities associated with the tunneling spin-mixing magneto-resistance effect, their change of behavior as topological defects due to different “vacuum background states” such as the ferro-, antiferromagnetic or helical state, thus stimulating the development of new theoretical concepts and methods, the exploration of new stable particles such as the anti-skyrmion and the bobber, as well as opening novel means of all-electrical skyrmion injection, manipulation, transportation and detection in a device context. All-in-all skyrmions and skyrmionics make-up an exciting and innovative field of science, that takes part in the general revolution condensed matter undergoes by notions of topology, that requests fundamental understanding of the quantum mechanical response of skyrmions to external electric and magnetic fields as manifested e.g. in various texture-driven spin and electronic transport effects, that meets information technology and in which density functional theory (DFT) plays a very important role. In this highlight, we review a scale-bridging approach relating the electronic structure to materials specific atomistic and micromagnetic interaction parameters responding to the quest for magnetic skyrmions with tailored properties, discussing methods for the treatment of spin-textures of one to hundred nanometers in size, introducing the hybrid-particle named bobber and discussing ballistic and topological transport properties for the electron detection of skyrmions.

[†]g.bihlmayer@fz-juelich.de

1 Introduction

Condensed matter physics is currently undergoing a revolution through the introduction of concepts arising from topology that are used to characterize physical states, fields and properties from a completely different perspective. With the introduction of topology, the perspective is changed from describing complex systems in terms of local order parameters to a characterization by global quantities, which are measured nonlocally and which endow the systems with a global stability to perturbations. A prominent example are skyrmions. Since topology translates into quantization and response and transport properties, this ongoing revolution has impact on fields like mathematics, physics, materials science and nanoelectronics resulting in new device concepts and ultimately reaching out into applications. Thus, these new exciting scientific developments and their applications are closely related to the grand challenges in information and communication technology and energy saving.

Thus, the quest for fundamental understanding of chiral magnetic skyrmions [1] with complex magnetic real-space topologies, their quantum mechanical responses to external static perturbations, their robust dynamics, their dependence on the background magnetization, the search for additional particles move skyrmions into center of intense scientific investigations. The topological protection of their magnetic structure and particle-like properties and stability [2] (for a review see Ref. [3]) with a well-defined topological charge offer good conditions for skyrmions to become the new information-carrying particles in the field of spintronics [4], which explains the additional motivation of their current intensive investigation. Skyrmions in chiral magnets may appear as isolated topological solitons or condensed in regular lattices. Their stability results from the Dzyaloshinskii-Moriya interaction (DMI) [5, 6], which breaks the chiral symmetry of the magnetic structure. The energy and size is determined by the competition between the Heisenberg, Dzyaloshinskii-Moriya, and Zeeman interaction together with the magnetic anisotropy energy (MAE) and the magnetostatic dipolar self-energy. But without DMI, chiral magnetic skyrmions do not exist. The DMI results from the spin-orbit interaction and is only non-zero for solids lacking bulk or structure inversion symmetry. Its strength depends on the degree of symmetry breaking experienced by the wave functions and can be modified by band filling or crystal field gradients or interface dipoles, respectively, due to the choice of chemical elements.

In terms of skyrmionics, i.e. when we consider the skyrmions as information-carrying particles in a novel technology that combines the ultrahigh data density of non-volatile storage device with the ultra-low power and fast operations of logic components, the skyrmions offer a great potential, not only due to their stability but also due to the presence of a quantized topological charge, a quantized topological orbital moment [7], emergent electrodynamics [8], a topological Hall effect (THE) [9] and the tunneling spin-mixing magneto-resistance (TXMR) [10, 11] opening means of detecting skyrmions in a device context, the lower pinning field in comparison to conventional domain walls [8] combined with the large spin-orbit torques (SOT) [12] exerted on the skyrmions, which conversely requires much smaller current densities than conventional magnets [13, 14].

Although the potential is great, the presently available skyrmions do not fulfill yet all required criteria for such a technology. The skyrmions should be stable sub-10 nm skyrmions at room temperature, (ii) should exhibit controlled and low power (sub-100 fJ) skyrmion nucleation using

current or electric field as writing process (iii) electrical detection of sub-10 nm skyrmion as reading process (iv) controlled, reliable and fast (over 1000 m/s) manipulation of the skyrmions trains in nanotracks of a potential race track memory [4] and (v) controlled skyrmion-skyrmion interaction to achieve logic operations.

This poses a challenge to materials design in general and DFT-based material and process understanding and design in particular: Chiral magnetic skyrmions have spin-orbit-driven non-collinear spin textures of several nanometers size that result from a fine balance of different magnetic interactions. To capture these effects with sufficient accuracy pushes DFT codes and computational resources easily to their limits. The electronic and spin-structure determine important transport properties.

The presence of skyrmions in bulk crystals and interfaces has been shown and verified experimentally, primarily in bulk crystal of noncentrosymmetric crystals of B20 alloys as MnSi [15], FeGe [16]; thick films of noncentrosymmetric B20 crystals with the thickness in a range between several tens up to few hundreds nanometers [17, 18, 19]; epitaxial films of noncentrosymmetric crystals – films of B20 alloys usually grown on thick Si substrate, e.g. MnSi/Si(111) [20, 21] or FeGe/Si(111) [22, 23]. For applications in spintronics [4, 24, 25] skyrmions stabilized in systems with surface or interface induced DMI seem to be more promising than bulk systems with DMI.

Magnetic heterostructures consisting of a thin film of magnetic material on a heavy metal substrate are a basis for the generation of skyrmions smaller than five nanometers [26, 27] that can e.g. be used as bits in a magnetic racetracks. Experimentally, it has been shown that individual bits can be created by an out-of-plane current and moved by an in-plane one [28, 29]. To read out the state of each bit, it has been shown that the topological Hall effect [30] can be utilized. Experimentally, this current-in-plane detection was already demonstrated [31]. In terms of device geometry and power consumption, a current-perpendicular-to-plane detection would clearly be advantageous [32]. The tunneling spin-mixing magnetoresistance effect is one mechanism that allows this type of detection [10, 11].

During the past 10 years we developed a consistent three-pronged scale-bridging approach for a material specific description of the static and dynamical properties of skyrmions. This approach consists of (i) the density functional model to relate the quantum mechanics of the relativistic electrons in a non-collinear magnet to exchange parameters entering (ii) a generalized spin-lattice model with local magnetic moments residing on the atom positions interacting through the well-known Heisenberg interaction, the Dzyaloshinskii-Moriya interaction and the magnetic anisotropy which comprises the magnetocrystalline anisotropy and the dipolar fields. (iii) The long wave-length limit or the continuum approximation of the atomistic model leads to the micro-magnetic model, where the magnetization density is a continuous field consistent with the mathematical concepts behind topology. The so obtained atomistic or micromagnetic model, respectively, is frequently named *ab initio* atomistic model or *ab initio* micromagnetic model.

We realize the DFT model through the community code named FLEUR, (<http://www.flapw.de>), an all-electron full-potential linearized augmented plane wave method devised such as to obtain all necessary parameters entering the spin-lattice or the micromagnetic model [33, 34]. We have developed several other first-principles methods to deduce the atomic interaction parameters and even to calculate small skyrmions as a hole from first-principles [10] based on the Korringa-

Kohn-Rostoker Greenfunction method (<http://www.juDFT.de>). In order to calculate the phase-diagram, the dynamical properties and the temperature dependent stability of skyrmions we are developing a user-friendly community code named `Spirit` (<http://spirit-code.github.io>), which is based on solving the Landau-Lifshitz Gilbert equation for the generalized spin-model. The transport properties of skyrmions were obtained with the Wannier interpolation technique based on the maximally-localized Wannier functions as constructed from the Wannier90 code (<http://www.wannier.org>) using the electronic structure output of FLEUR [35].

In this article we cover some of the aspects mentioned above addressed with density functional theory and methods that build up on DFT results. In the first part, we discuss a two-scale approach relating first-principles calculation of the electronic structure of non-collinear states to magnetic stability and size of a skyrmion through spin-lattice model. Presented are the calculations of magnetic interaction parameters, e.g. Heisenberg-type or Dzyaloshinskii-Moriya interactions, higher order terms and the magnetic anisotropy that can serve as input for Monte-Carlo simulations or spin-dynamics simulations. While we chose skyrmions in thin-film systems as examples here, in the next chapter novel topologically stabilized objects in three dimensions, so called bobbers, hybrid-particles of Blochpoint singularities with a continuous skyrmion-like spin-texture and their continuum modeling is in the focus. In chapter 4 we return to the thin-film systems and outline methods for the calculation of single skyrmions as a whole entity from first principles. This allows addressing the spatial variation of the electronic structure and we will discuss possible mechanisms for the electrical detection of skyrmions, important for the read-out of data stored with these magnetic structures. The topological Hall effect is another electronic signature of skyrmions. Its calculation from DFT for ferro- and antiferromagnetic skyrmions is the topic of the final chapter.

2 Magnetic interactions from first principles

Magnetic skyrmions are noncollinear magnetic structures that, for DFT, very often require substantial efforts since calculations of large magnetic unit cells with inclusion of relativistic effects are needed. Compared to a collinear, scalar-relativistic calculation, the size of the Hamiltonian is doubled in this case and the computational efforts increases typically by a factor four to eight. Since such straightforward calculations are not always feasible, we first shortly review some methods to explore the magnetic structure of a given material (or composite) and, as illustrative example, show how the nanoskyrmion lattice of Fe on Ir(111) was discovered as a combined experimental and theoretical effort.

To determine the magnetic ground state of a specific system by DFT is a rather challenging problem: Let us assume that at the positions of the magnetic atoms the intra-atomic exchange interaction is large and there are robust magnetic moments that can be assigned to each lattice site, e.g., within some sphere centered at the nucleus, i (at a position \mathbf{R}_i), the magnetization density, $\mathbf{m}(\mathbf{r})$, can be well approximated as

$$\mathbf{m}(\mathbf{r}) = M_i \hat{\mathbf{e}}_i \tag{1}$$

where M_i is the magnetization and $\hat{\mathbf{e}}_i$ is the magnetization direction at that site. Then, a magnetic state is characterized by a set of directions, $\{\hat{\mathbf{e}}_i\}$, of all the atoms in the magnetic unit

cell. Of course, there are the well-known ferromagnetic (FM) and antiferromagnetic (AFM) states, but already for the latter several possible unit cells come in mind. E.g., in an face-centered cubic (fcc) material, an AFM order can occur for ferromagnetically ordered planes in (001), (111), or (110) directions (type I, II or III AFM order, respectively) to name just the few possibilities that can be realized by a Heisenberg model with nearest-neighbor (nn) and next-nearest-neighbor (nnn) interactions. With more Heisenberg-type interactions involved, so-called spiral spin-density waves (SSDW) are general solutions:

$$\mathbf{M}_i = M (\hat{\mathbf{e}}_x \cos(\mathbf{q} \cdot \mathbf{R}_i) + \hat{\mathbf{e}}_y \sin(\mathbf{q} \cdot \mathbf{R}_i)) \quad (2)$$

where \mathbf{M}_i is the magnetic moment of atom i and the unit vectors $\hat{\mathbf{e}}_x$ and $\hat{\mathbf{e}}_y$ just have to be perpendicular to each other, otherwise their directions are arbitrary. For simplicity we assume that the size of the magnetic moment, M , is not site dependent. Using the generalized Bloch theorem [36, 37] these SSDWs can be conveniently calculated in the chemical unit cell as long as no spin-orbit coupling (SOC) is considered. For our calculations we use the full-potential linearized augmented plane-wave (FLAPW) method [38] as implemented in the FLEUR-code [39].

In a DFT calculation (as well as in nature) exchange interactions are not limited to Heisenberg-type, J_{ij} , ones: even in the non-relativistic (NR) case higher order exchange interactions (biquadratic, \mathcal{B}_{ij} , or four-spin, \mathcal{K}_{ijkl} , interactions) can couple SSDWs to new spin structures. E.g. in a Heisenberg chain with biquadratic interaction, a so-called up-up-down-down structure can appear as ground state that is a superposition of two counterpropagating spin-spirals [40]. In the Mn monolayer on a Cu(111) substrate we found a superposition of three SSDWs to form a so-called $3\mathbf{Q}$ ground state [41]. But, of course, it is difficult to prove that a certain solution obtained in a DFT calculation gives really the energy minimum as supercell-effects always affect the results. Thus, the situation is similar to the problem of structural relaxation, only on a much smaller energy scale: The energy functional $E[\{\hat{\mathbf{e}}_i\}]$ has many local minima that differ typically by just a few meV. Therefore, ab-initio spin-dynamic simulations are in principle a good way to explore magnetic ground states [42, 43], but computationally rather expensive. Moreover, for an interpretation of the results usually the system is mapped to a model Hamiltonian, e.g.

$$\begin{aligned} H_{\text{NR}} = & - \sum_{\langle ij \rangle} J_{ij} \mathbf{M}_i \cdot \mathbf{M}_j - \sum_{\langle ij \rangle} \mathcal{B}_{ij} (\mathbf{M}_i \cdot \mathbf{M}_j)^2 \\ & - \sum_{\langle ijkl \rangle} \mathcal{K}_{ijkl} [(\mathbf{M}_i \cdot \mathbf{M}_j)(\mathbf{M}_k \cdot \mathbf{M}_l) + (\mathbf{M}_j \cdot \mathbf{M}_k)(\mathbf{M}_l \cdot \mathbf{M}_i) - (\mathbf{M}_i \cdot \mathbf{M}_k)(\mathbf{M}_j \cdot \mathbf{M}_l)] \end{aligned} \quad (3)$$

to explain a certain ground state structure and look for competing spin configurations if a suitable phase diagram is available. Although the sums in eq. 3 run in principle over all pairs or quadruples (diamonds), depending on the number of performed DFT calculations these sums are truncated rather quickly. In particular the biquadratic and four-spin terms are assumed to decay much faster than the Heisenberg-type terms and only few are considered: for each exchange interaction constant an independent spin-texture, often requiring a special magnetic unit cell, is required [44]. In contrast, the J_{ij} parameters can be determined rather systematically based on SSDW calculations using the generalized Bloch theorem [45].

The situation gains complexity if relativistic terms, in particular arising from SOC, are taken into account [46]. Including just the Dzyaloshinskii-Moriya interaction (DMI) [5, 6], the magnetic

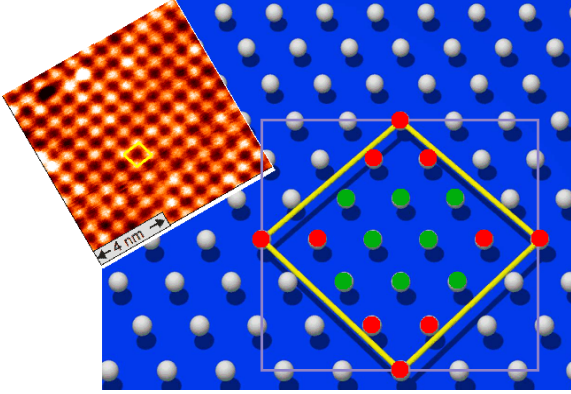


Figure 1: Upper left inset: experimentally obtained SP-STM image of the Fe monolayer on Ir(111). The magnetic unit cell (yellow) contains 15 surface atoms. To explain the magnetic contrast, a collinear structure with the spin of eight atoms pointing up (green) and seven atoms pointing down (red) would be possible. A $c(2 \times 2)$ supercell is indicated in gray. (Adapted partially from Ref. [51])

anisotropy (arising from SOC and dipole-dipole interaction) and the interaction with an external magnetic field, the Hamiltonian is expanded to

$$H = H_{\text{NR}} - \sum_{\langle ij \rangle} \mathbf{D}_{ij} \cdot (\mathbf{M}_i \times \mathbf{M}_j) + \sum_i \mathbf{M}_i \mathbf{K}_i \mathbf{M}_i + \sum_i \mathbf{B} \cdot \mathbf{M}_i \quad (4)$$

where H_{NR} is given by eq. 3, \mathbf{D}_{ij} is the Dzyaloshinskii-vector, \mathbf{K}_i the anisotropy tensor and \mathbf{B} the (external) magnetic field. In the case of a uniaxial anisotropy and out-of-plane magnetic field the last two terms simplify to sums over $K_i(M_i^z)^2$ and BM_i^z , respectively. The contribution of the magnetocrystalline anisotropy to the \mathbf{K} tensor can be extracted from (usually collinear) relativistic calculations with an extremely fine \mathbf{k} -point grid over the Brillouin-zone. The dipole-dipole terms are usually added from a classical calculation of the dipole sums using the calculated magnetic moments.

The DMI contribution can be evaluated e.g. from SSDW calculations using the generalized Bloch theorem and considering SOC in first order perturbation theory [47]. In this case, for each \mathbf{D}_{ij} vector three independent non-collinear calculations including SOC effects are necessary (although symmetry considerations [6] help to ease the computational effort). As the energy differences between these magnetic configurations are in the meV range, also here carefully converged calculations requiring several thousand \mathbf{k} -points are necessary. This applies also to calculations of the DMI via Green function methods [48] or Berry phase theory [49].

2.1 Nanoskymions at surfaces

To give an actual example for the rather abstract discussion above, we look at the system of an Fe monolayer on an Ir(111) substrate. Experimentally obtained images with spin-polarized scanning tunneling microscopy (SP-STM) are shown in the inset of Fig. 1: Obviously, there is an almost square magnetic unit cell with a lattice parameter of about 1 nm dominating the contrast [50]. Assuming an epitaxial growth of the Fe, the chemical unit cell is expected to be hexagonal with an in-plane lattice constant of about 0.27 nm. This implies that the magnetic unit cell consists of 15 atoms as shown in Fig. 1. A magnetic structure, possibly compatible with the SP-STM image, obtained with an out-of plane magnetized tip, could consist of eight atoms with spin pointing up and seven with spin pointing down as indicated by the red and green circles. DFT calculations confirm that this structure has indeed a lower energy than the ferromagnetic state and all tested SSDW solutions [50].

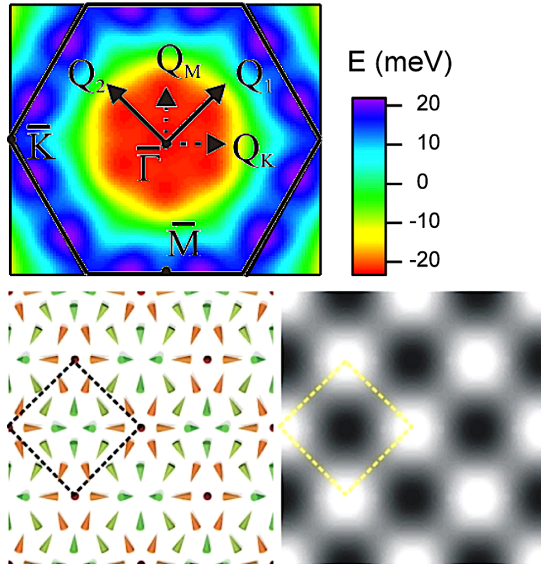


Figure 2: Upper panel: Total energy of spin-spiral states in an Fe monolayer on Ir(111). Although the FM state has the lowest energy, there is a wide plateau in the total energy surface, $E(\mathbf{q})$, where the spin-spiral energies are small. The vectors \mathbf{Q}_1 and \mathbf{Q}_2 are given by the Fourier-transform of the experimental SP-STM image (see Fig. 1). The multi-Q state shown in the lower image is formed by the spin-spirals with these \mathbf{q} -vectors and \mathbf{Q}_M . Red and green color of the arrows indicates out- or in-ward pointing moments, respectively. The simulated SP-STM image (lower right) matches the experimental ones quite well. (Adapted from the supplementary (SI) information of Ref. [53])

Of course, there are many other magnetic structures compatible with the experimental result shown in Fig. 1, indeed experimental evidence indicated that the situation might be more complex: From further investigations it was concluded that the magnetic structure is fully compensated, i.e. the total spin moment of the Fe layer is zero [51]. Given the fact that the Fe moments are rather robust ($M_{\text{Fe}} = 2.96 \pm 0.06 \mu_B$), this is incompatible with any collinear structure in a 15 atom unit cell. Therefore, it was speculated that the structure could be slightly non-collinear, but at that time we were not able to find a non-collinear magnetic solution with an energy lower than the collinear 7 + 8 structure.

Let us consider the exchange interactions in the hexagonal Fe monolayer: without any substrate or on a weakly interacting substrate like Ag(111), Fe is strongly ferromagnetic and, in nnn-approximation, the exchange constants are $M^2 J_1 = 23.6$ meV and $M^2 J_2 = -3.1$ meV for Fe at the Ag(111) lattice constant [52]. Upon interaction with a substrate like Ir(111) these values are reduced to 4.2 meV and -0.8 meV, respectively [44]. This puts the Fe/Ir(111) close to the phase transition from the FM state to a spin-spiral along the line $\Gamma - M$ that connect the FM to a row-wise AFM state. Actually, the spin-spiral spectrum shows that there is a shallow plateau, about 10 meV above the FM state, in all spin-spiral directions (see Fig. 2) [50]. It is located at about $q = 0.25(2\pi/a)$ which is compatible to the observed magnetic lattice constant of about 1 nm. Here, a is the Ir(111) in-plane lattice constant and we consider that the magnetic period length is given by $\lambda = (2\pi)/q$.

Up to now we considered only exchange interaction effects that are included in scalar relativistic DFT calculations. Taking into account also SOC, the SSDWs can gain additional energy due to the DMI as given in eq. 4. In the presence of one dominant nearest-neighbor term, \mathbf{D}_{01} , it favors a flat spin-spiral with an angle of 90° between neighboring spins. Usually, exchange interactions terms lead to more long-ranged modulations, in addition a certain sense of rotation is selected, as observed e.g. in Mn monolayers on W(110) [54].

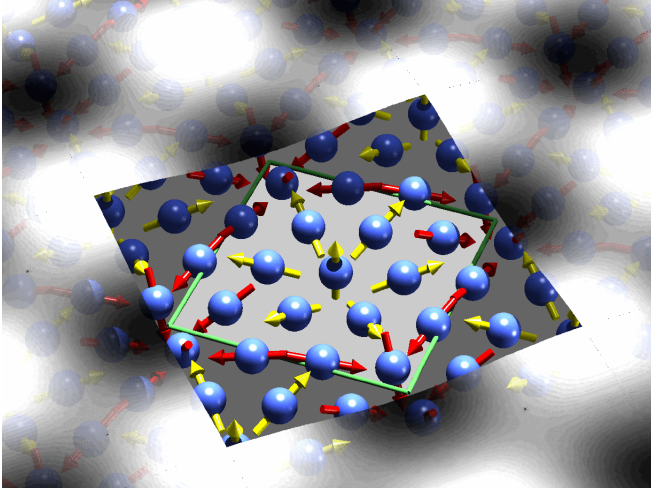


Figure 3: Visualization of the nano-skyrmion lattice of Fe on Ir(111): The blue spheres represent Fe atoms, magnetic unit cell is outlined in green. The seven yellow arrows in the middle form the skyrmion motive, which is responsible for the white areas in the simulated SP-STM image (the simulation for an out-of plane magnetized tip is overlaid on the atomic structure).

To obtain a two-dimensionally modulated spin structure it is necessary to combine SSDWs with different \mathbf{q} vectors: As mentioned above, higher order spin interactions can lead to so-called multi- \mathbf{q} states described as $\mathbf{M}_n = \sum_{\nu} \mathbf{M}_{\nu} e^{i\mathbf{q}_{\nu} \cdot \mathbf{R}_n}$. For this, it is not only necessary that the higher order interaction favors this state, but also the magnetic moment \mathbf{M}_n should be constant and the vectors \mathbf{q}_{ν} should correspond to low-energy solutions in the spin-spiral spectrum. In the ideal case of the above-mentioned $3\mathbf{Q}$ state of Mn on Cu(111), the three \mathbf{q}_{ν} vectors are row-wise AFM states on the hexagonal lattice, rotated by 120° with respect to each other. In the case of Fe on Ir(111) one can choose three vectors from the shallow plateau of the spin-spiral spectrum to form a multi- \mathbf{q} state [53]. The state formed from \mathbf{Q}_1 , \mathbf{Q}_2 , and \mathbf{Q}_M indeed shows a two-dimensionally modulated structure with the right periodicity (Fig. 2).

DFT calculations show that this multi- \mathbf{q} structure is energetically favored as compared to the lowest-energy single- \mathbf{q} state. Although it loses some energy due to unfavorable alignment of the spins for Heisenberg-type exchange and DMI, it wins enough energy to compensate for that. Looking at the spin-structure in Fig. 2, we see that the red arrows form groups of seven spins, each, that are arranged like tiny skyrmions or anti-skyrmions. Such magnetic structures have been predicted recently [55], but in the present system only the star-shaped nanoskyrmion (same rotational sense of the spins in both in-plane directions) can gain energy from the DMI. Therefore, it is a rather logical next step to modify the magnetic structure by replacing all anti-skyrmions in the lattice with skyrmions. This gives another gain in energy, mainly caused by DMI and the cyclic 4-spin interaction, giving rise to the nanoskyrmion lattice ground state (shown together with the simulated SP-STM image in Fig. 3) of Fe on Ir(111) [53]. We note here that experimentally there is a small incommensurability of the magnetic lattice with the underlying atomic structure, a situation which is computationally expensive to simulate in DFT calculations but it is a nice demonstration of the stability of the skyrmionic ground state.

A few remarks on the details of the DFT calculations for this system are in order here: (1) in the calculations, the surface is simulated by an Fe monolayer on a thin film of Ir(111). Systematic studies for different (Ir) film thicknesses show that the obtained magnetic interaction parameters depend rather sensitively on the number of Ir layers. Moreover, the stacking of Fe on the Ir(111) substrate (fcc/hcp) changes these parameters as can be observed both in theory and in experiment [56]. (2) These results also depend sensitively on the relaxation of Fe on the

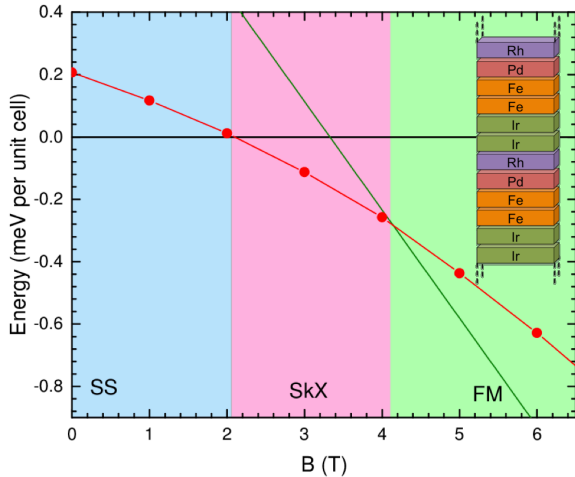


Figure 4: Phase diagram of the magnetic ground state of an Rh/Pd/2Fe/2Ir multilayer as visualized in the inset. The energy of the SSDW state (SS) is the black line used as reference energy. The energy of the FM state and the skyrmion lattice (SkX) are given in green and red, respectively. The energies are determined by Monte-Carlo simulations with parameters as given in the text. (Adapted from the SI of Ref. [27])

Ir substrate. DFT simulations of the relaxation of $3d$ metals on $5d$ substrates can be quite misleading since GGA functionals tend to overestimate the lattice parameters of the substrate, while LDA functionals underestimate the exchange splitting of the $3d$ atoms (and the associated magneto-volume effect) [57]. Here, we circumvented that problem by choosing the experimental Ir lattice parameters and relaxing just the Fe layer in GGA. (3) The GGA functionals have the tendency to yield too low energies of antiferromagnetic structures, often favoring AFM ground states where experimentally non-collinear ordering is found [58]. Therefore, we determined our exchange interactions using an LDA functional.

2.2 Multilayer structures

In the last subsection, we discussed how interactions described by the Hamiltonian (4) can stabilize a skyrmion lattice in absence of magnetic fields. Of course, this requires a subtle balance between the individual terms in this Hamiltonian and, due to the short-ranged nature of the higher-order interactions, only small-scale skyrmions can be expected. Indeed, it was realized soon after the discovery of the nanoskyrmion lattice that a Pd layer on top of Fe/Ir(111) stabilizes a spin-spiral ground state. However, with a small external magnetic field (1.4 T) out this state nanometer-sized skyrmions evolve [26, 59, 60]. Indeed, it can be shown that a Hamiltonian of the form

$$H = - \sum_{\langle ij \rangle} J_{ij} \mathbf{M}_i \cdot \mathbf{M}_j - \sum_{\langle ij \rangle} \mathbf{D}_{ij} \cdot (\mathbf{M}_i \times \mathbf{M}_j) + \sum_i K_i (M_i^z)^2 + \sum_i B M_i^z \quad (5)$$

gives rise to skyrmions when the magnetic field is in the right range. As shown in Fig. 4, below or above that range the system is in a SSDW or FM ground state, respectively.

As we have seen above, an important ingredient for the formation of two-dimensionally modulated structures is a range of low-energy spin-spiral solutions around the FM state (see Fig. 2). From our studies of Fe/ $4d$ interfaces [44], we know that the Heisenberg-type exchange interactions can be tuned by the $4d$ material from FM to AFM nature. The same is true for Fe/ $5d$ interfaces, but this interface effectively also controls the DMI [61]. If we form a $4d$ /Fe/ $5d$ multilayer structure, this gives us two (almost) independent tuning knobs to engineer magnetic skyrmions [27]. We consider here structures with two Fe layers sandwiched between the non-magnetic transition metals, to increase also the temperature stability of the skyrmions. Apart

from their stability, these structures have many advantageous properties for data storage and processing, e.g. they can be driven by an electric current or be utilized in three-dimensional storage concepts.

	$M^2 J_1^{\parallel}$	$M^2 J_2^{\parallel}$	$M^2 J_3^{\parallel}$	$M^2 J_4^{\parallel}$		$M^2 D_{\text{eff}}$	
Fe@Ir	-1.70	0.36	-1.53	0.03	Ir	1.5	
Fe@Pd	3.67	0.56	-0.84	0.20	Pd	-0.3	
	$M^2 J_1^{\perp}$	$M^2 J_2^{\perp}$	$M^2 J_3^{\perp}$	$M^2 J_4^{\perp}$			$M^2 K$
Fe-Fe	27.42	0.24	-0.40	-0.60	Fe	0.1	1.5

Table 1: Model Hamiltonian parameters for Rh/Pd/2Fe/2Ir. The exchange constants are obtained from fitting the energy dispersion of spin spirals calculated via DFT calculations. The Heisenberg-type interactions are separated into an intra-layer J^{\parallel} and an inter-layer part J^{\perp} , the DMI contributions from the different layers are shown separately in the right column. The uniaxial anisotropy K is obtained from collinear DFT calculations with SOC included. All units are in meV.

As example, we focus here on the Rh/Pd/2Fe/2Ir multilayer shown in the inset of Fig. 4. The exchange parameters are given in Table 1. It can be clearly seen that the exchange coupling in the Fe layers is very weak, while the coupling between the layers is significant. Therefore, if a skyrmion is formed, it shows the same radial profile in both layers (see Fig. 5). We can also see that J_3 is relatively large. As the Hamiltonian (5) contains no higher-order interaction terms, it is well possible that biquadratic interactions were mapped into the J_3 term. While a fit of eq. 5 to a SSDW calculation (without field and SOC) directly gives intra- and inter-layer parts of the J 's, to separate the J^{\parallel} into contributions of different layers needs further calculations: For this, we perform SSDW calculations where the magnetization of one Fe layer rotates with a flat spin-spiral around the z -axis while the other layer has the magnetization fixed in z -direction. This gives access to layer-resolved quantities - although the contributions are not strictly additive (e.g. $M^2 J_1^{\parallel} = 3.86$ meV obtained from a SSDW calculation with spirals in both layers), the individual trends can be inferred.

As for the DMI, we characterize it here by a single number D_{eff} . It is obtained by fitting the SOC contribution to the total energy (obtained by first order perturbation theory as shown in Ref. [47]) of spin-spirals with period λ in $\bar{\Gamma} - \bar{K}$ direction to an energy term $E_{\text{SOC}} = D/\lambda$ (the anisotropy K_i vanishes in first order perturbation theory). Thus, only the x -component of \mathbf{D}_{eff} is obtained, the y -component, extracted from SSDW in $\bar{\Gamma} - \bar{M}$ direction, is almost identical. From the layer-decomposition of D one can clearly see that the scattering on Ir gives the dominant contribution. Let us note here, that the spin-orbit contribution to the total energy can be written as a sum over atomic sites, α :

$$E_{\text{SOC}} = \sum_{\alpha, \mu} \langle \Psi_{0, \mu} | H_{\text{SOC}} | \Psi_{0, \mu} \rangle_{\alpha} \quad (6)$$

where $\Psi_{0, \mu}$ is the wavefunction of band μ of the SSDW state without SOC and H_{SOC} is the SOC operator. The integration $\langle \rangle_{\alpha}$ is performed over non-overlapping atomic spheres, which makes the separation of the atomic contributions possible.

Given the model Hamiltonian parameters as listed in Table 1, it is possible to study the skyrmion

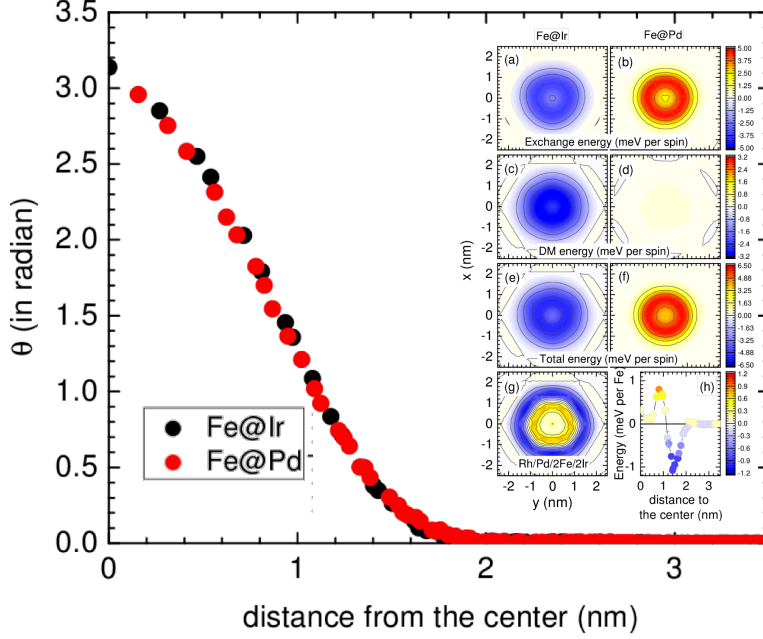


Figure 5: Skyrmion profile and energy contributions for Rh/Pd/2Fe/2Ir multilayers. θ is the angle of the magnetization in the two Fe layers with the z -axis. The inset gives the total energy contributions of the symmetric exchange (a,b) and DMI (c,d) and the total energy per layer (e,f). Panel (g) and (h) show the radial distribution of the skyrmion, site resolved and averaged over the shells, respectively. (Adapted from the SI of Ref. [27])

formation in an external magnetic field by spin-dynamics simulations [27]. Apart from the profile (size) of the skyrmion, shown in Fig. 5, also the energy contributions of the individual terms of eq. 5 can be analyzed in a site-resolved fashion: As shown in the insets (a) and (b) of Fig. 5, the Heisenberg-type exchange favors the spin-rotation in the Fe layer near Ir (as expected from the negative J_1^{\parallel} in Table 1) but disfavors the rotation at the Pd interface. On the other hand, insets (c) and (d) show that only at the Ir interface a significant energy gain can be obtained from the DMI. Adding the external field and the anisotropy, one sees that in a region close to the center energy is lost by skyrmion formation, mainly due to the exchange terms near the Pd interface, while DMI favors the spin-rotation in a wider range, up to 2 nm from the center. Inset (h) shows the radial distribution obtained by averaging over equidistant atoms (shells) from the center of the skyrmion. In total, it is the DMI term dominating between 1 nm and 2-nm distance that stabilizes this magnetic structure.

Summarizing this section, we tried to show how DFT calculations of magnetic interaction parameters can help to tailor material systems for the formation of skyrmions. E.g. the size of skyrmion or the critical magnetic field, where the skyrmion lattice forms, can be tuned via the exchange constants J and D and the magnetic anisotropy by designing the interfaces to $4d$ and $5d$ materials. How this affects the temperature stability will be discussed more in the next section. We discussed homogeneous, two-dimensional periodic systems here and did not include edge-effects, defects etc. and their interaction with skyrmions, also this will follow later. Although focused on layered magnetic systems, the general principles outlined here are also applicable to bulk materials that form skyrmions, most prominently the family of B20 compounds.

3 Magnetic skyrmions and new particlelike objects in cubic chiral magnets

Cubic chiral magnets (ChMs) belong to a distinct class of magnetic crystals where – contrary to the classical ferro- and antiferromagnets – the ground state represents a noncollinear state. To this class of magnetic materials belong different Si- and Ge-based alloys such as MnSi [62] and FeGe [63], $\text{Mn}_{1-x}\text{Fe}_x\text{Ge}$ [64], $\text{Mn}_{1-x}\text{Fe}_x\text{Si}$ [65], $\text{Fe}_{1-x}\text{Co}_x\text{Si}$ [17]. The broken inversion symmetry of such alloys with B20 crystal symmetry together with strong spin orbit coupling gives rise to the Dzyaloshinskii-Moriya interaction (DMI) [5, 6]. Such alloys can be referred to as isotropic chiral magnets. Such a classification reflects the dominant role of DMI and Heisenberg exchange, which are assumed to be isotropic in all spatial directions, while the contribution of magnetocrystalline anisotropy can be neglected. The special interest to such materials arose after the breakthrough results on the first direct observation of magnetic skyrmions in thin films of $\text{Fe}_{0.5}\text{Co}_{0.5}\text{Si}$ [17]. The experimental discovery of magnetic skyrmions together with the conceptual idea of a revolutionary new type of magnetic memory gave an additional impetus to the research in this field [24, 4].

The competition between ferromagnetic exchange interaction and the DMI results in the ground state representing a incommensurate homochiral spin spiral – the spiral with an unique sense of magnetization rotation, see Fig. 6(a). The equilibrium period of such a spin spiral, L_D , is governed by the competition of exchange stiffness and DMI [66]. In a bulk sample, the spin spiral usually appears as a multidomain state, with a set of spiral \mathbf{k} -vector directions across domains [67]. In the presence of a homogeneous applied magnetic field, \mathbf{H} , such a multidomain spiral state transforms into a monodomain conical state, with the magnetization \mathbf{M} tilted towards the direction of the external field and with $\mathbf{k} \parallel \mathbf{H}$, Fig. 6b-c. The conical state persists as the lowest energy state over the entire range of applied magnetic fields up to a critical value of H_D , above which it converges to a saturated ferromagnetic state.

The existence of the magnetic skyrmions in magnetic crystals with DMI has been theoretically predicted by Bogdanov in 1989 [1], but it took more than twenty years to discover them experimentally. One of the reasons behind this late discovery is the modification of the conventional energy balance in thin films of ChMs in comparison to the bulk crystals. Indeed, according to the theory developed by Bogdanov and co-workers, see e.g. Ref. [21], the chiral skyrmion tubes, see Fig. 6(d), in bulk crystals of ChMs with relatively weak magnetocrystalline anisotropy may appear only as a metastable state. Their energy is always higher than the energy of the conical phase, which dominates in bulk crystals almost in the whole range of magnetic fields and temperatures. This result is consistent with many experimental studies on bulk ChM over the past decades, where skyrmions were not observed. The only exception is the so-called A-phase – the high-temperature region in the bulk phase diagram, just below the ordering temperature, where skyrmions have been proposed to exist due to thermal fluctuations [15]. However, the real nature of the A-phase still is under debate [15, 68, 16]. The theoretical models predict that in bulk crystals of ChMs, the magnetic skyrmions can be stabilized due to the strong cubic or uniaxial anisotropy [21, 69] or special crystal symmetry, which suppress the formation of the conical phase [1, 70]. However, such theoretical models as well as thermal fluctuations can not be considered as the main mechanism for skyrmion stabilization in stand-alone thin films of

B20-alloys where the skyrmions are observed in a wide range of temperatures, much lower than the ordering temperature.

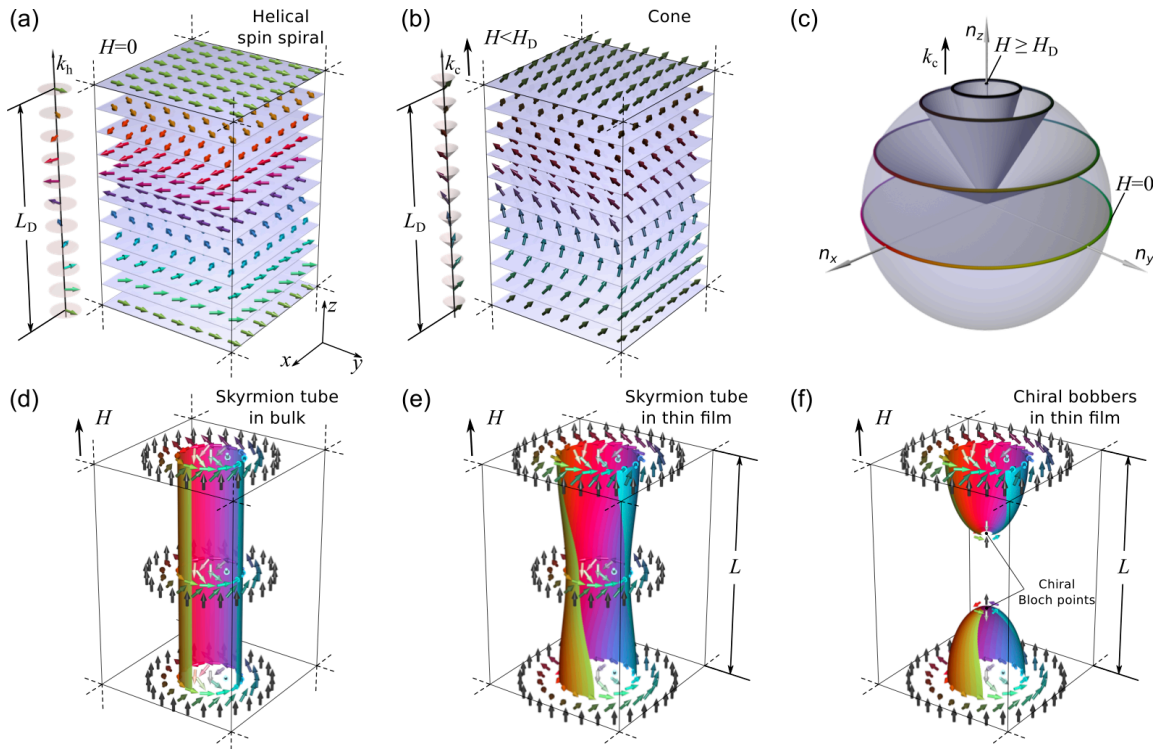


Figure 6: Schematic representation of different modulated states in bulk and thin films of chiral magnets: (a) Helical spin spiral at zero field with wave vector \mathbf{k} pointing along the z -axis. (b) Conical state with inclined magnetization and wave vector along the magnetic field. (c) The projections of the spins on unit sphere corresponding to helical spin spiral ($H = 0$) and conical spin spiral ($0 < H < H_D$) with \mathbf{k} -vector pointing along external field $\mathbf{H} \parallel \mathbf{e}_z$. (d)–(f) The vector field and cross sections of corresponding isosurfaces, $n_z = 0$, for: skyrmion tube with homogeneous magnetization along the radial symmetry axis (d), for skyrmion tube in thin film of chiral magnet with inhomogeneous magnetization in all three spatial directions and the twist induced by the free surface (e), chiral bobbers – hybrid particle-like states localized near the surface of the chiral magnet characterized by smooth magnetization distribution and presence of singularity – chiral Bloch point at finite distance from the surface (f), for details see Section 3.4 and Ref. [71]. Note, the section of the isosurfaces in (d)–(f) corresponds to $n_y > 0$, $n_x < 0$.

As has been shown in Ref. [72] the key to the understanding of the mechanism of skyrmion stabilization in thin films of ChM are presence of the free surfaces and the three-dimensional rather than the two-dimensional structure of the equilibrium skyrmions. As shown in Fig. 6(e), the solution for the skyrmion tube in a thin film is characterized by the twist of magnetization with respect to the normal vector of the film surfaces. One can compare the twisted isosurface of the skyrmion tube in Fig. 6(e) and the homogeneous non-twisted skyrmion tube in (d). The magnetic moments in the top surface layer are slightly turned towards the center of the skyrmion, while in the bottom of the film they are slightly turned outwards the center. The spin structure on the top and bottom surfaces corresponds to a certain intermediate configuration in between of pure Bloch- and Néel-type of skyrmions. Such surface induced twist propagates from one

surface to another through the whole film. Note, it mainly affects the magnetic spins near the surfaces where spins are weakly coupled to each other because of reduced number of neighbors at the free surface. Far from the film surface, the spin structure of such a 3D skyrmion remains almost the same as in a homogeneous skyrmion tube.

The energy gain by the DMI contribution accumulated along the film thickness reduces the total energy of the state such that within a certain range of magnetic fields and film thicknesses the skyrmion tube becomes energetically more favorable than the conical phase. Moreover, it has been shown earlier that the same effect is responsible for the stability of chiral bobber – particlelike objects localized in all three spatial directions near the surface of the chiral magnet, Fig. 6(f), see also section 3.4.

It is obvious that for very thick films, the relative energy contribution of the surface twist becomes very small, while the main contribution to the energy of skyrmion comes from the volume part of the film. Thereby, there should be a critical thickness above which the energy gain of the surface twist is not anymore sufficient to provide enough energy gain to stabilize a skyrmion lattice. In order to identify the range of thicknesses and magnetic fields defining the range of stability for the skyrmion lattice and other states, we have calculated a phase diagram for the film of isotropic ChM in a wide range of thicknesses and applied magnetic fields, which is presented in section 3.2.

3.1 Basic model of isotropic chiral magnet

The basic model for isotropic chiral magnet include three main energy terms: the Heisenberg exchange interaction, the DMI and Zeeman energy term [73, 74]:

$$\mathcal{E} = \mathcal{E}_0 + \int_V \mathcal{A} \left(\partial_x \mathbf{n}^2 + \partial_y \mathbf{n}^2 + \partial_z \mathbf{n}^2 \right) + \mathcal{D} \mathbf{n} \cdot [\nabla \times \mathbf{n}] + H M_s (1 - n_z) d\mathbf{r}, \quad (7)$$

where $\mathbf{n} \equiv \mathbf{n}(\mathbf{r})$ is a continuous unit vector field defined everywhere except at the singular points. \mathcal{E}_0 is the energy of the saturated ferromagnetic state. \mathcal{A} and \mathcal{D} are micromagnetic constants for exchange and DMI, respectively, and M_s is the magnetization of the material – the total magnetic dipole moment per unit volume.

The constants of exchange stiffness, \mathcal{A} , and DMI, \mathcal{D} , for B20-type chiral magnets, in general, can be found from the first principles calculations has been discussed in section section 2. As compared to the two-dimensional systems, the high symmetry in the discussed bulk compounds changes the relative importance of the interactions and some are rather challenging to access quantitatively throughout the mentioned B20 compounds, but DFT certainly allows to study interesting trends e.g. in the DMI values of $\text{Mn}_{1-x}\text{Fe}_x\text{Ge}$ [75, 76, 77].

We use the continuum model as the most general approach to describe long-period incommensurate magnetic structures. The results presented here can be easily generalized for a wide class of the systems. The functional (7) has to be considered as a continuum limit for the classical spin models e.g. as simplified models considering a simple cubic lattice [78], and advanced models, which take into account the exact B20 crystal symmetry [79, 80].

The lowest period of an incommensurate spin spiral and equilibrium period of the conical phase, L_D , as well as the critical field corresponding to the saturation field of the conical phase, H_D , have

analytic solutions, which couple the material parameters with quantities that can be calculated in DFT or measured experimentally [66, 70]:

$$L_D = 4\pi \frac{\mathcal{A}}{\mathcal{D}}, \quad H_D = \frac{\mathcal{D}^2}{2M_s \mathcal{A}}. \quad (8)$$

The comparison of the energy density of each of the equilibrium states obtained by direct energy minimization of the functional (7) allows one to identify the geometrical and material parameters corresponding to the phase transitions. The details of the energy minimization technique and calculation of the phase diagram are provided in Ref. [81].

3.2 Phase diagram

In the phase diagram presented in Fig. 7 the thickness of the film, L , and magnetic field H are given in reduced units, where L_D and H_D are the functions of material parameters \mathcal{A} , \mathcal{D} and M_s , see Eq. (8). The unique pair of parameters L_D and H_D can be considered as a *fingerprinth* of each particular IChM. They can be measured experimentally, which allows to rescale the phase diagram, Fig. 7(a), in real units of film thickness, L and magnetic field H .

The solid lines in Fig. 7 correspond to the first-order phase transitions between helical spin spiral (red), skyrmion lattice (gray), conical phase (white) and a new, up-to-now unknown phase, which we call *stacked spin-spirals state* (yellow) and is discussed in detail in section 3.3. The horizontal dashed line indicates the second order phase transition between conical and saturated ferromagnetic state (blue).

The triple point I defines the critical thickness of the film, $L^* = 8.17L_D$, above which the skyrmions may exist only as a metastable state. For instance, for MnSi ($L_D = 18$ nm) and FeGe ($L_D = 70$ nm) it gives $L_{\text{MnSi}}^* \approx 150$ nm and $L_{\text{FeGe}}^* \approx 570$ nm. With decreasing thickness the range of existence for the skyrmion lattice in an applied magnetic field becomes wider. This fact reflects the relative contribution of the surface induced twists, which increases with decreasing thickness. There is another critical point, for $L/L_D < 0.68$, the conical phase is totally suppressed and becomes energetically unfavorable in the whole range of fields.

It is important to mention that the chiral surface twist discussed above also introduces an additional modulation in the helical spiral state. Note, the \mathbf{k} -vector of such helical spiral lies in the plane of the film, orthogonal to the applied field. The surface induced modulation reduces the energy of the helix and in a certain range of fields makes it energetically more favorable than the conical state. Such a behavior of the system is totally different to the one of the bulk crystals, where theoretically any infinitesimal magnetic field leads to convergence of the helix to the conical phase or more precisely to the StSS according to results presented here, see right panel in Fig. 7.

Finally, we have to emphasize that the effect of the chiral surface twist is not restricted to the film surfaces, but also appears on the side edges of the sample. The presence of the edge twist effect has been reported earlier in Ref. [20] and has been confirmed recently by direct observation with the Lorentz Transmission Electron Microscopy (TEM) [18].

It is worth to emphasize that the continuum 3D model of chiral magnet strictly speaking does not converge to a simple 2D model even in the limiting case of $L/L_D \rightarrow 0$. The left panel

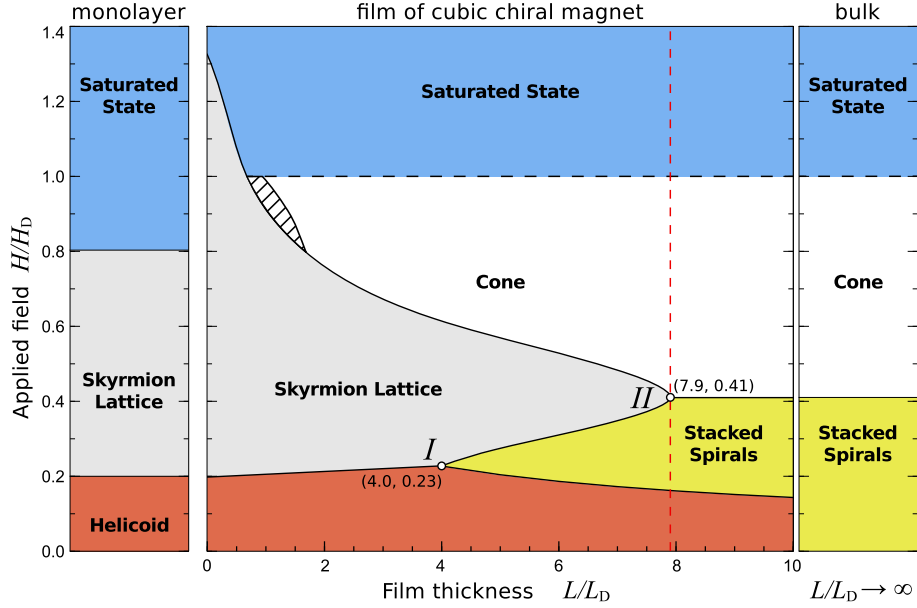


Figure 7: The phase diagram of magnetic states in film of isotropic chiral magnets: (a) The phase diagram of magnetic states in reduced units of film thicknesses L and magnetic field H applied normally to the film surface. The central panel corresponds to the reduced film thickness varied between 0 and $L = 50L_D$ (L_D is the period of helicoid at $H=0$). Inset shows details of the phase diagram for thin films, $0 < L \leq 10L_D$. Note, everywhere within the range of stability of the conical phase, the isolated chiral bobber corresponds to the lowest metastable state, the only exception is the small dashed area, where isolated skyrmions within the conical phase become the metastable state with the lowest energy. The left panel corresponds to the case of monolayer with surface induced DMI. The right panel corresponds to the case of infinitely thick film, which qualitatively corresponds to the bulk crystal. Small open circles marked as I and II , with corresponding coordinates indicated as $(L/L_D, H/H_D)$ correspond to the triple-points. The vertical (red) dashed line indicates the critical thickness above which skyrmions appear only as metastable state.

in Fig. 7(a), which corresponds to the phase diagram of 2D chiral magnet illustrates such a discrepancy. Note, in general 2D models are valid not only for the single monolayer but also for multilayer with interface induced DMI and for chiral magnets of particular crystal symmetry e.g. C_{nv} , D_{2d} and S_4 [1, 70].

3.3 Stacked spin spirals

A wide range of the phase diagram is occupied by the newly found stacked spin spirals state (StSS). The triple point II defines the limiting thickness above which the StSS may appear as the global energy minimum.

Fig. 8 illustrates the complex spin structure of the StSS obtained by direct minimization of the functional (7). The StSS represents the coexistence of the conical phase in the bulk of the sample and the quasi-helical modulation of magnetization localized in the vicinity of the surface of the sample. Such free surface induced modulations have finite penetration depth and appear on both the top and bottom surfaces. It exhibits a mixed helical- and cycloidal-like modulation,

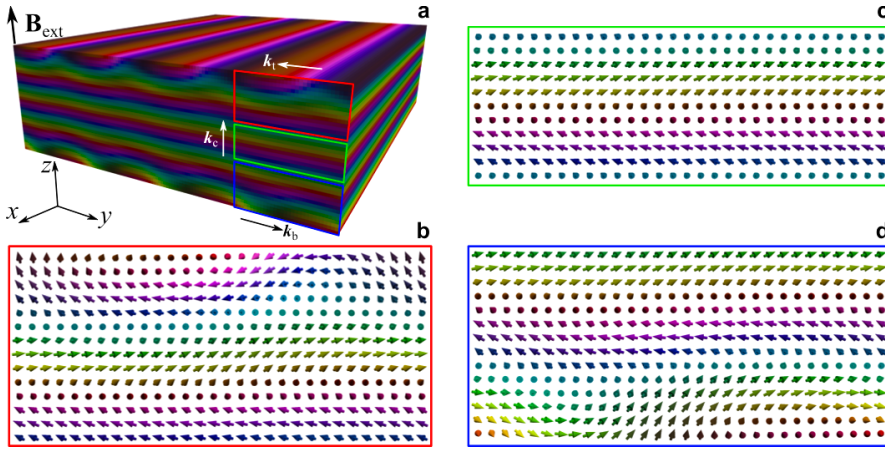


Figure 8: Stacked spirals states: (a) The magnetization distribution for the stacked spin spirals in the film of cubic chiral magnet with the thickness of $L = 4L_D$ and external field applied normally to the film plane. The local magnetization direction is indicated by the colors according to the standard color code, see Fig. 6 c. (b)-(d) The magnetization vector field near the top surface of the film (b), in the middle part of the film with pure conical modulations (c) and near the bottom surface (d). \mathbf{k}_c indicates the propagation direction of the conical spiral in the bulk of the film, while \mathbf{k}_t and \mathbf{k}_b indicate the propagation directions of the complex spin spirals on the top and bottom surfaces, respectively. Note, for the thickness $L = 4L_D$ the vectors \mathbf{k}_t and \mathbf{k}_b are anti-parallel and both are orthogonal to \mathbf{k}_c . In this particular case, the configuration corresponds to the lowest energy state.

Fig. 8b,d. The clock-wise rotation of magnetization in the helical-like part is chosen as direction of the wave vector \mathbf{k} for such a complex spin spiral.

It has been found that the relative orientation of the propagation vectors of the spin spirals on the top and bottom surfaces, \mathbf{k}_t and \mathbf{k}_b , respectively, is thickness dependent. In other words, the angle β_{tb} between \mathbf{k}_t and \mathbf{k}_b for the equilibrium StSS in general varies as function of the film thickness. Note, that this statement is valid only for the case when stray field effect is neglected.

The modulation of the out-of-plane component of the magnetization of the surface spin spiral should lead to appearances of the stray fields above the sample, which in turn can be detected by Magnetic Force Microscopy (MFM) in films as well as in bulk crystals. However, with an ordinary MFM technique it seems to be hard to distinguish the StSS from the ordinary helical state, which also produces a stray field around the sample. The most promising experimental technique, which may allow to detect the StSS seems to be Lorentz TEM.

3.4 Magnetic chiral bobbbers

Despite the fact that the presence of the DMI in chiral magnets commonly prevents the stability and coexistence of topological excitations of different types, recently it was theoretically predicted that magnetic skyrmions in cubic chiral magnets can coexists with another new type of localized particle-like object – the chiral bobber (ChB) [71]. ChB is a three-dimensional soliton of the nonlinear equations for a unit vector field. On the other hand ChB represent a hybrid

particle composed of a smooth magnetization vector field and a magnetic singularity (Bloch point). Fig. 6f illustrate a pair of ChB localized near the top and bottom surfaces; however, due to the mutual repulsion of Bloch points energetically more preferable is appearance of isolated ChBs.

In the cross section with the plane parallel to the layer surface, its spin structure mimics the magnetization distribution of the skyrmion with the diameter diminishing with distance from the surface. It has been shown that the value of the penetration depth, P of ChB always satisfies the condition $PL_D/2$ with an accuracy up to one unit cell of crystal lattice. The term chiral bobber is used because of the essential chirality of its spin texture and due to the fact that as such it is localized close to the surface of the sample and in a certain sense behaves like a fishing bobber on the waters surface.

It turns out that due compact size of ChBs in a wide range of parameters they are energetically more favorable than the chiral magnetic skyrmions. Note, everywhere in phase diagram, Fig. 7 within the range corresponding to the cone ground state an isolated ChB represents a measurable state with the energy lower then the energy of isolated SkT. The only exception represents small dashed region at high magnetic field and small thicknesses where isolated SkT has energy lower than that of isolated ChB.

In Ref. [71] it has been shown that the energy barriers that protect skyrmions and ChBs are of the same order of magnitude and the two objects are potentially ideal candidates for use as “1” and “0” bit carriers, Fig. 9. Indeed, although magnetic hard disk drives show great reliability and are some of the most in-demand devices on the market, their ultimate data density and operating speed are limited due to the superparamagnetic effects [82] and the presence of energy-consuming mechanical components, such as engines and actuators. Therefore, alternative approaches for solid state magnetic memory devices that have no movable mechanical parts have been proposed. One of the most promising candidates for a new solid-state magnetic memory device is based on the concept of racetrack memory (RM) [83], in which the role of data bit carriers is played by either (i) magnetic domain walls, which are small transition regions between domains whose magnetization typically points in opposite directions [83] or (ii) chiral magnetic skyrmions [24], which possess topologically protected stability and can be moved using currents that are several orders of magnitude lower than those required for magnetic domain wall motion [4]. Skyrmion-based RM is currently considered to be the most promising approach.

The presence of only one type of excitation currently defines the approach for data encoding, which is based on the quantization of distances between adjacent excitations on a track. However, skyrmions are highly movable, interacting objects that can drift as a result of thermal fluctuations, making it difficult to maintain their distribution along a track. The fabrication of arrays of artificial pinning centers on the nanoscale to solve this problem is a serious challenge that is likely to lead to higher costs. In a system with surface/interface-induced DMI, a solution is the fabrication of a nanostripe with a special profile that results in the location of skyrmions in two parallel channels [84].

A powerful alternative approach, which does not require fixed distances between movable bit carriers has been proposed in Ref. [85]. It is proposed that the stream of binary data representing a sequence of ones and zeros can be encoded via a sequence of two type of movable particles,

for instance skyrmions and bobbers. In this approach, the need to maintain defined distances between data bit carriers is then not required. The coherent motion of ChBs and SkTs is expected to be stable because of cohesion effects due to interparticle interactions. The conceptual scheme of a single register in such a memory device is shown in Fig. 9. The proposed concept of data encoding promises to expedite the realization of a new generation of magnetic solid-state memory, where a higher data density can be achieved in comparison to the existing skyrmion-based racetrack memory concept.

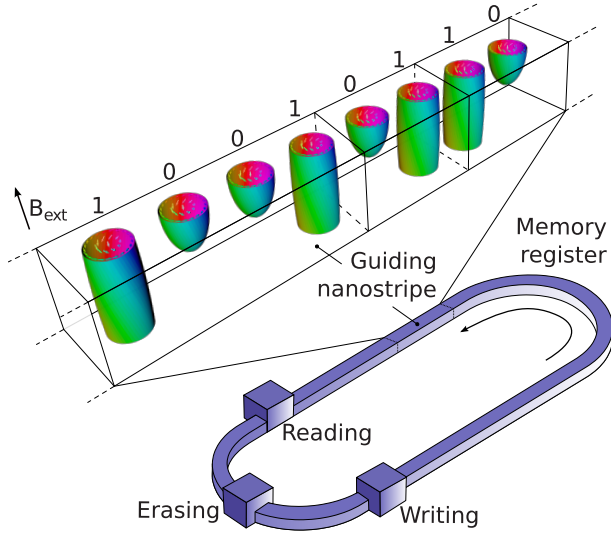


Figure 9: New concept for magnetic solid-state memory based on encoding a data stream in a nanostripe, which takes the form of a closed track containing a chain of alternating magnetic skyrmion tubes and chiral bobbers that correspond to “1” and “0” bits. The actions of writing, reading and erasing units are performed at different positions along the guiding track. The spin structures for chiral bobbers and skyrmion tubes are schematically represented by corresponding isosurfaces. The figure is adapted from Ref. [85].

4 Single skyrmions from full first-principles

In this section, we address simulations based on full ab-initio of single magnetic skyrmions, which allows direct access to the details of their electronic structure, spin and orbital magnetic textures and transport properties. As mentioned in the introduction, from the technological perspective it is probably more interesting to generate and harness individual skyrmions than a lattice of skyrmions. For instance, single sub-5nm skyrmions, i.e. nano-skyrmions, are ideal for a racetrack memory device. Although computationally heavy, such first-principles simulations can have direct implications in device concepts. For example, a novel magnetoresistance effect, which we named spin-mixing magneto-resistance (XMR), was put forward to be used for efficient all-electrical detection of non-collinear spin-textures (see Fig.10(a) and Ref. [10]). This effect was simultaneously realized and addressed experimentally and theoretically in Ref. [11]. Another example consists in proposing a way of accessing the topological nature of a complex spin-texture by measuring with optical means the orbital moment generated by the non-collinearity of the magnetic moments [7, 86]. Such a contribution to the total orbital moment inherits the

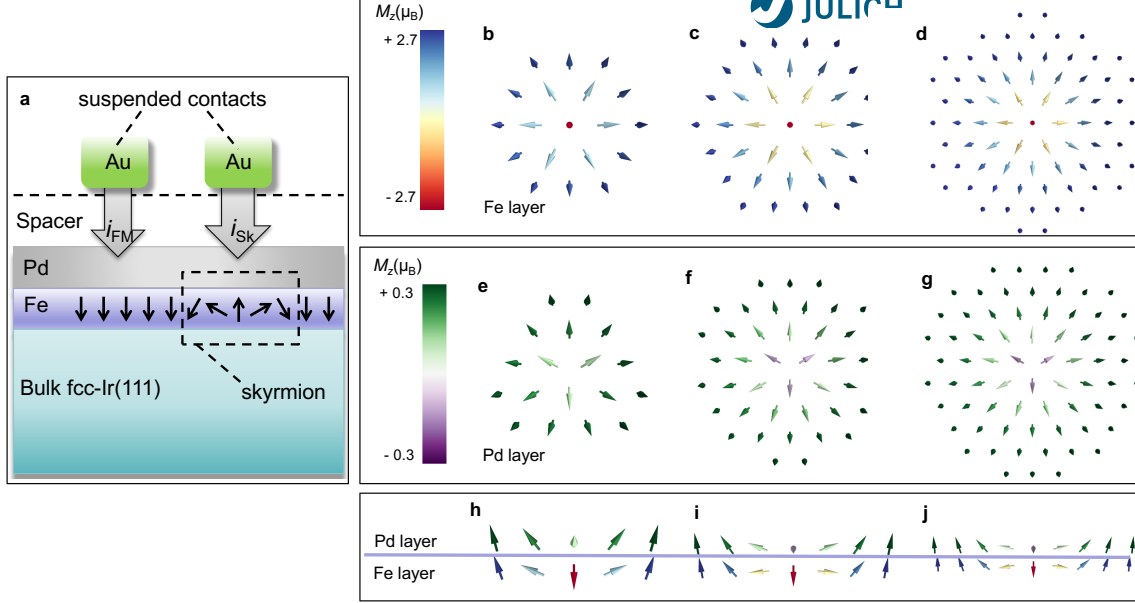


Figure 10: (a) Illustrative concept for a device based on perpendicular reading of single nano-skyrmions. Due to spin-mixing of the electronic structure as a function of position within skyrmions, the electric current, i , depends on the local magnetic state, leading to a spin-mixing magnetoresistance (XMR) and therefore magnetic data information can be sensed in a CPP-geometry. (b-j) Ab-initio relaxed skyrmions of different sizes generated in fcc-Pd/Fe overlayer on fcc-Ir(111) bulk substrate. The top-view of the magnetic textures located in the Fe-layer are shown in b-d and in (e-g) for the Pd-overlayer. The Pd magnetic moments are mainly induced and controlled by the underlying magnetic Fe layer. A comparison between the two textures can be grasped from the side views shown in (h-j).

topological nature of magnetic skyrmions and is thus called the topological orbital moment [7]. Here we review the work presented in Ref. [10] by showing data calculated with higher energy resolution. The simulation of a single magnetic skyrmion embedded in an otherwise perfect magnetic substrate requires the use of a Green functions based technique. For such problems, self-consistent calculations based on the full-potential relativistic Korringa-Kohn-Rostoker Green function formalism are possible [87]. To stabilize skyrmions, the Green functions of the ferromagnetic substrate are harvested and a single spin-flipped magnetic-atom is embedded in the unperturbed ferromagnetic background. The potentials of the nearest neighboring atoms surrounding the skyrmion are updated till self-consistency is reached. The procedure is based on a multiple scattering approach to solve the Dyson equation: $G_{\text{skyrmion}} = G_0 + G_0 \Delta V G_{\text{skyrmion}}$ in real space, where ΔV represents the modified atomic potential as compared to the unperturbed substrate potential. G_0 is the Green function of the perfect substrate while G_{skyrmion} represents the skyrmion impurity cluster.

Similar to section 2, we consider once more the case of an Fe fcc-monolayer on an Ir(111) substrate, on top of which a single Pd-layer or -bilayer are deposited following for simplicity an fcc stacking. In such materials with strong magnetic frustration, Pd overlayers enhance the ferromagnetic Heisenberg exchange, which stabilizes spin-spirals over the skyrmionic lattice. A reasonable magnetic field, however, generates isolated skyrmions with diameter $D_{Sk} \approx 1-5$ nm

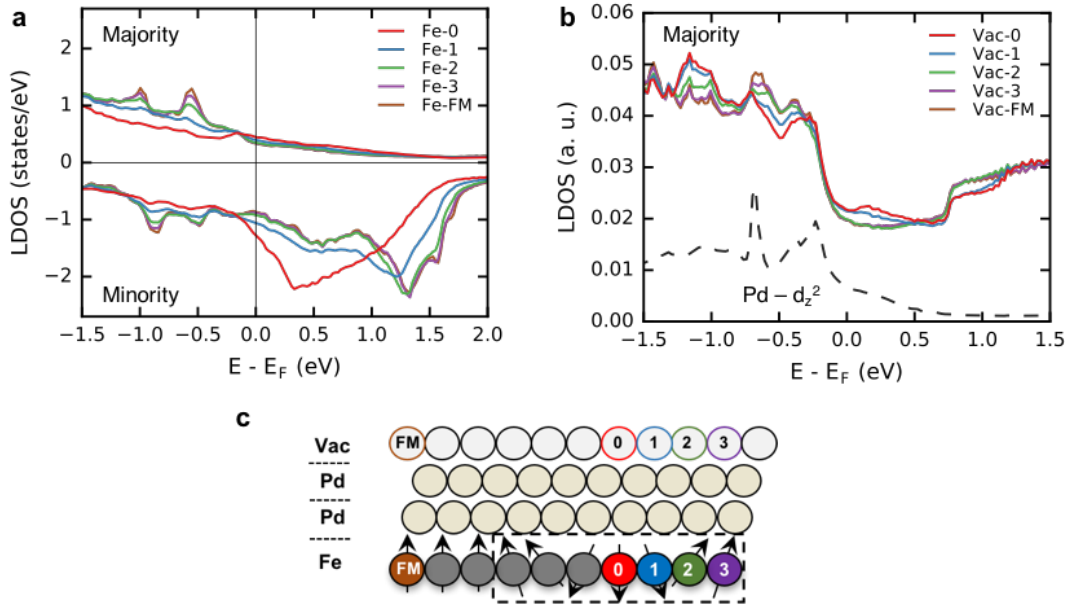


Figure 11: LDOS in a realistic 2.2 nm wide nano-skyrmion in $Pd_2/Fe/Ir$. (a) Electronic structure in the magnetically-active Fe-layer resolved into minority (solid) and majority (dashed) spin-channels changes across the skyrmion from the ferromagnetic (FM) background towards the skyrmion's core characterized by a quasi-antiferromagnetic (AFM) alignment of the moments. (b) The alteration of the LDOS in Fe impacts the vacuum structure via hybridization through Pd-states. Arbitrary units are used so as to include in the same plot the nature of the $Pd - d_{z^2}$ surface-state (black-dashed). (c) Illustrative legend for (a,b) where the numbered spheres represent a line extending radially from the skyrmion's center. The vacuum domains are represented by empty spheres. FM-Fe, FM-Pd, and FM-Vac represent the unperturbed background ferromagnet.

in size, and has been shown experimentally [11, 26, 88, 89]. We note that in the context of thin films possibly hosting small skyrmions, new systems have recently been proposed theoretically, such as PtIr alloy deposited on Fe/Ir(111) surface [90, 91] and Mn monolayer deposited on $/W/Co/Pt/W(001)$ [92], or discovered experimentally such as the Fe triple layer deposited on Ir(111) [93].

In practice, we used a slab containing 34 Ir layers since it was the minimum thickness by which we completely decoupled any wave function penetration from top-to-bottom surface. Relaxations are incorporated using the data reported by Dupé *et al.* [59]. We chose an angular momentum cutoff of $l_{max} = 3$ for the orbital expansions of the Green functions. The energy contour for numeric integration of the spin and charge density contained 40 grid points in the upper complex plane (including 7 Matsubara poles) with a Brillouin zone mesh of 30×30 k -points. The local density of states (LDOS) were obtained by one-shot calculations using the ferromagnetic-state or skyrmion-state as starting points, respectively. We found that increasing the k -mesh to 200×200 was sufficiently adequate to numerically stabilize the relevant observables.

4.1 Non-collinear inhomogeneity in nano-skyrmions

Fig. 10(b-j) shows the self-consistent magnetic texture for different-sized nano-skyrmions generated in otherwise ferromagnetic single Pd overlayer material stacks. Results obtained for the Pd-bilayer are rather similar and not shown for brevity; see Ref.[10] for a comparison with the single Pd layer case. As expected, the DMI imposes a unique rotational sense for the magnetic moments. We control the size of the skyrmionic defects, having a diameter $D_{\text{Sk}} \approx 1.1, 1.7, 2.2,$ and 2.7 nm, by allowing different finite numbers of atoms to relax their magnetic moments in size and direction after the central atom has been spin-flipped as an initial condition. The skyrmions are not confined to the Fe layer but extend towards the Pd overlayer and Ir substrate (not shown). The generated magnetic textures are dictated by Fe, which induces magnetism in Pd and Ir via a proximity effect.

We show in Fig. 11a the spin-dependent LDOS in the magnetically-active Fe-layer as a function of the atomic position for the $D_{\text{Sk}} \approx 2.2$ nm skyrmion. For brevity we plot only the Pd₂/Fe/Ir case. We note that the majority and minority spin-channels are given in the local spin-frame of reference for each Fe-atom. The color-coding of the plot, which corresponds to different atoms extending radially from the skyrmion's center, is explained in Fig. 11c. Obviously, the LDOS changes as function of the location of the Fe atom within the nano-skyrmion. Because of the specific nature of the skyrmionic spin-texture, Fe atoms across the skyrmions are inequivalent making the local magnetic environment inhomogeneous. For instance, the minority-spin electronic bands observed in Fig. 11a shift in energy as function of position. The essential physics behind this process can be explained on the basis of the Alexander-Anderson model [94, 95] extended to the case of non-collinear spin-structures [10]. When moving from the ferromagnetic background towards the center of the skyrmion, the quantization axis between two neighboring atoms becomes different, and majority-states of one atom can hybridize with minority-states of its neighbors. This affects the effective hybridization strength between the electronic states of adjacent atoms and thus the final electronic structure.

4.2 Angular dependence of the LDOS across nano-skyrmions

$\Delta n_i(E)$ denotes the change in the LDOS at site i inside an inhomogeneous non-collinear spin-texture with respect to a fixed magnetic moment. The latter can be pointing along the z -direction if located in the ferromagnetic background surrounding our skyrmions. $\Delta n_i(E)$ originates from the spin-orbit interaction (SOI) and/or from non-collinearity (NC): $\Delta n_i(E) = \Delta n_i^{\text{SOI}}(E) + \Delta n_i^{\text{NC}}(E)$. The contribution from SOI, the so-called anisotropic magnetoresistance, is well known:

$$\Delta n_i^{\text{SOI}}(E) \propto A(r, E) \cdot [1 - (\hat{e}_i^z)^2] \quad , \quad (9)$$

where $A_i(E)$ is a site- and energy-dependent coefficient and \hat{e}_i defines the direction of the magnetic moment at site i . Thus upon including SOI, we expect, for example, a $\sin^2 \theta_i$ dependence, which contributes to $\Delta n_i(E)$ in second-order.

Even when SOI is ignored, NC induces changes in the electronic structure across a skyrmion since the atoms are not necessarily equivalent. This effect holds true for any inhomogeneous spin-texture. Multiple-scattering theory enables to relate the Green function G , describing the

whole system upon rotation of the magnetic moments, to the Green function g , describing the initial ferromagnetic state, via the Dyson equation:

$$\Delta G = g\Delta V G = g\Delta V g + g\Delta V g\Delta V g + \dots, \quad (10)$$

where ΔV describes the change of the potential upon rotation of the magnetic moments. The change in the LDOS can then easily be extracted from:

$$\Delta n_i^{\text{NC}}(E) = -\frac{1}{\pi} \Im \left\{ \text{Tr}_{\text{LS}}[G^{ii}(E) - g^{ii}(E)] \right\}, \quad (11)$$

as given in a matrix notation where a trace over orbital and spin angular momenta has to be performed.

Using properties of Pauli matrices and limiting the sum in Eq. 10 to the first- and second-order terms, we find:

$$\Delta n_i^{\text{NC}}(E) = \sum_j B^{iji}(E)(1 - \hat{e}_j^z) + \sum_{jk} C^{ijk}(E)[\hat{\mathbf{e}}_j \cdot \hat{\mathbf{e}}_k - (\hat{e}_j^z + \hat{e}_k^z) + 1], \quad (12)$$

where j and k are sites surrounding site i , or can be the site i itself and the coefficients B and C depend on G and ΔV (more details can be found in Ref.[10]). Thus we obtain a rather complex dependence on the rotation angles of the magnetic moments, very distinct from the expected SOI contribution. Of course, depending on the details of the electronic structure and strength of perturbation related to the non-collinearity, higher-order terms can be important and have to be included in Equation 12.

4.3 All-electrical skyrmion detection

The energy-dependent disturbance to the LDOS resonance-peaks as a function of position moving radially along the skyrmion implies that it will leave a non-trivial signature in the electrical conductivity of a probed skyrmion. Current-in-plane (CIP) detection of skyrmions has been already shown experimentally [8, 31, 96] and understood theoretically as a topological Hall effect [9], but may be costly in terms of power consumption and difficult to fabricate in terms of device geometries. A better option would be the direct detection of the nano-skyrmions via current-perpendicular-to-plane (CPP) [32, 97] geometry. The latter can be realized within the context of scanning tunneling microscopy/spectroscopy (STM/STS), as shown recently in the context of the present work [10, 11, 89], which can be simulated using the Tersoff-Hamann model [98]. In the latter model the differential conductance dI/dV is proportional to the LDOS of the sample, calculated at the STM-tip position. An example is shown in Fig. 11b for $\text{Pd}_2/\text{Fe}/\text{Ir}(111)$, where electronic features of the majority-spin channel at negative or positive bias voltages change across the 2.2 nm nano-skyrmion, some of which originate from the VBS characterizing the Fe atoms hybridizing with the states of Pd, which then decay into the vacuum. The states involved in the hybridization processes and their energy location depend strongly on the Pd film's thickness and the size of the skyrmion. In the particular case of a Pd bilayer, hybrid Fe-Pd- spd_{z^2} states, named in short Pd- d_{z^2} , are generated in the Pd layers around -0.5 eV, as shown in Fig. 11b (black-dashed curve). It is clear that the surface-layer Pd- d_{z^2} state (shown only for the background-FM Pd-surface film), which has the proper orbital

symmetry to decay slowly transverse to the substrate, controls the electronic structure in vacuum at negative bias voltage, characterized by a strong resonance in the vacuum-LDOS. In the case of a single Pd overlayer, a similar state occurs around +0.5 eV [10]. Thus the changes in the electronic structure induced by SOI and non-collinearity impact transport properties leading to the aforementioned XMR effect, or TXMR effect where T stands for tunneling.

The TXMR efficiency is the percent deviation of the local conductance from a reference conductance, which in our case is the ferromagnetic (FM) background, due to the spin-mixing arising from non-collinearity and SOI:

$$\text{TXMR}_i(E) = \frac{n_i^{\text{vac}}(E) - n_{\text{FM}}^{\text{vac}}(E)}{n_{\text{FM}}^{\text{vac}}(E)} \times 100, \quad (13)$$

where $n_{\text{FM}}^{\text{vac}}(E)$ is the LDOS in the vacuum just above the FM, and $n_i^{\text{vac}}(E)$ is the LDOS of the complex spin-texture in the vacuum just above site i .

Integrating the TXMR over the entire device injection boundary, over all energies up to the bias energy eV_{bias} , would give a measure of the total change in conductance, and would be the state-of-bit detection mechanism in a CPP-TXMR device like discussed in Fig. 10a. In an STS experiment, however, the effect could be amplified by selecting specific energy windows where the TXMR were largest as a function of position.

In Fig. 12a,b we show the energy-resolved TXMR of the $D_{\text{Sk}} \approx 2.2$ nm skyrmion's central spin-flipped vacuum-site, with and without SOI, for the single- and double-Pd cases. We notice a sizable TXMR effect for both systems. This holds true for all skyrmions that we studied, noting a small size-dependence of the effect which varies weakly as a function of D_{Sk} . When switching-off SOI and keeping the spin-texture fixed, the TXMR can differ by a factor of two with respect to what is found if SOI is included. This indicates that the spin-mixing due to SOI competes with the effects due to inhomogeneous non-collinearity, reducing or enhancing the overall TXMR signal. The experimentally investigated single Pd layer deposited on Fe/Ir(111) [11, 89] shows a TXMR signal similar to the one provided in Ref. [10]. As an example, the simulated TXMR signal for the double-Pd case is plotted in Fig. 12c at a bias energy -0.85 eV. In the future, it would be interesting to prospect the possibility of using the TXMR effect in the multilayers geometry, which is crucial in spintronics. Also, recent ab-initio simulations demonstrated the non-trivial impact of defects on the shape and stability of magnetic skyrmions [99]. Thus, it is appealing to study the sensitivity of the TXMR effect to the presence of defects.

5 Topological (spin) Hall effect of large-scale skyrmions

The variation of the spin texture in a skyrmion that a propagating (e.g. in response to an electric field) electron experiences has an influence similar to that of a magnetic field in real-space, which is given by the so-called real-space Berry curvature $\Omega_z^\sigma = -2\text{Im}\langle\partial_x\psi^\sigma(x,y)|\partial_y\psi^\sigma(x,y)\rangle$, where σ stands for the spin character of the ‘‘local’’ electronic wavefunction ψ in real-space. Without spin-orbit interaction the wavefunction has a trivial dependence on the (x,y) -coordinate via the local magnetization direction \mathbf{M} , and it can be shown that $\Omega_z^\sigma = \sigma \mathbf{M} \cdot (\partial_x \mathbf{M} \times \partial_y \mathbf{M}) / 2$. The curvature Ω_z^σ is often called an *emergent magnetic field*, B_{eff} . The integrated value of the emergent field over a skyrmion acquires integer values and is proportional to the winding

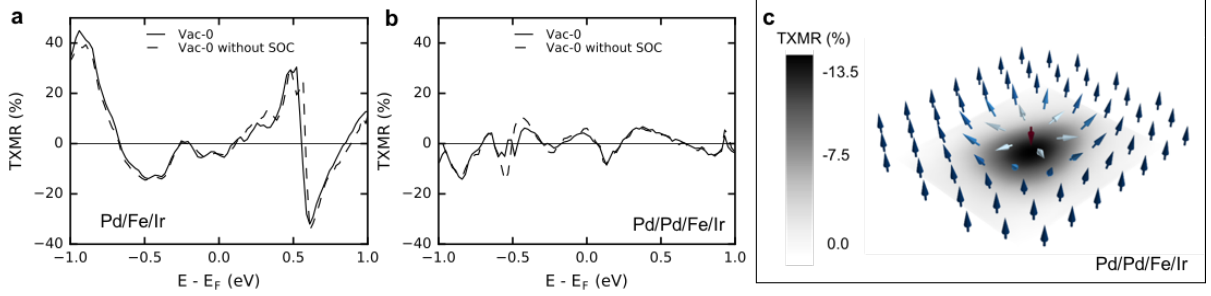


Figure 12: Tunneling spin-mixing magnetoresistance at the vacuum site, Vac-0, just above the core of the skyrmion (see Fig.11c). (a,b) TXMR signals comparing the effects of SOI in a $D_{Sk} \approx 2.2$ nm skyrmion, for single- and double-Pd systems. (c) Expected STS-signal when approaching a skyrmionic defect in the double-Pd case. The electrical contrast has been projected onto the plane below the skyrmion.

number:

$$S = \frac{1}{4\pi} \int \mathbf{M} \cdot (\partial_x \mathbf{M} \times \partial_y \mathbf{M}) dx dy. \quad (14)$$

The real-space Berry curvature is the magnetic field which changes sign depending on the spin of an electron. One of the consequences of having a magnetic field in the system is the Lorentz force which is exerted on electrons propagating in an electric field, which in turn gives rise to the ordinary Hall effect. In case of a spin texture, however, the emergent field gives rise to a Lorentz force which changes sign depending on the spin of an electron. The corresponding Hall effect, which is a specific feature of spin textures, is called the *topological Hall effect* (THE) [100, 101]. The topological Hall effect is a purely geometrical phenomenon in that it is driven by (adiabatically slow) modulation of the magnetic texture in space, and in that it can be written in terms of Berry curvature of spin-up and spin-down electrons, which sums up to zero when both spins are occupied. The magnitude of the emergent magnetic field at given point in space directly depends on how quickly the texture changes in real space. For example, in case of a skyrmionic lattice in MnSi, the winding number is -1 and given the skyrmion lattice constant of approximately 165 \AA , the magnitude of the emergent magnetic field can be estimated to be -13 T [102]. Nowadays, the THE is one of the main effects which is used to demonstrate the emergence of non-trivial spin textures in complex magnets. Correspondingly, the proper understanding of the THE of skyrmions opens the road to their purely-electrical manipulation and detection.

Spin textures in the presences of external fields show many emergent phenomena that are directly linked to the chirality and topology of the spin texture, such as the manipulation of the local magnetic moments through spin orbit torques [49], or coupling of the magnetic moments to the electric field in multiferroic materials. Through AMR and electrical resistivity measurements one can distinguish between the different directions of the order parameter of the magnetic system, while through the family of Hall effects, seemingly more complex in nature, one can directly probe the magnetic structure under the application of perpendicular external magnetic and electric fields. In addition to the THE, there are two more conventional effects that couple the charge current to the spin textures, i.e. the ordinary and anomalous [103] Hall effects, and the separation of the the three can be rather cumbersome. Each effect has a spin Hall counterpart

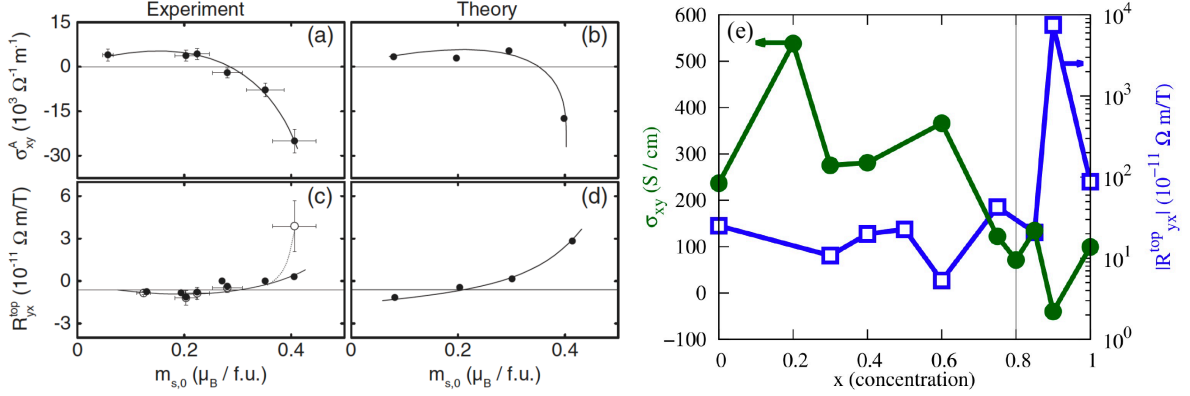


Figure 13: The topological and anomalous Hall effect in B20 alloys: In $\text{Mn}_{1-x}\text{Fe}_x\text{Si}$ alloys as a function of magnetization (i.e. as a function of x) a) the experimental AHE and b) the first principles AHE is plotted. c) the experimental topological Hall constant and d) the comparison to first principles results. e) The green curve is the AHE and the blue is the THE in $\text{Mn}_{1-x}\text{Fe}_x\text{Ge}$ varying with Fe alloying.

with zero net charge flow.

5.1 THE of ferromagnetic skyrmions

For large locally ferromagnetic spin textures it is normally assumed that experimentally the Hall resistivity can be separated into three “independent” contributions [31, 103]:

$$\rho_{xy} = \rho_{xy}^{\text{OHE}} + \rho_{xy}^{\text{AHE}} + \rho_{xy}^{\text{THE}} \quad (15)$$

Typically, in experiments, the ordinary Hall effect (OHE), $\rho_{xy}^{\text{OHE}} = R_0 H$ with R_0 as the ordinary Hall constant and H as the magnetic field, and the anomalous Hall effect (AHE), $\rho_{xy}^{\text{AHE}} = R_S M$ where R_S is the anomalous Hall constant, are fitted in the high field regime where M is saturated and the AHE dominates. The fitted results are then subtracted from the Hall resistivity for the whole range of the external magnetic field thus providing the values of the topological Hall resistivity, $\rho_{xy}^{\text{THE}} = R_{xy}^{\text{THE}} B_{\text{eff}}$ where R_{xy}^{THE} is the topological Hall constant which is weakly dependent on the shape of the skyrmions, and that exists in the range of H where there the emergent field B_{eff} is non-vanishing owing to the non-trivial winding of the real space magnetic texture. MnSi and FeGe in the B20 phase were among the first metallic materials that displayed the formation of a skyrmion lattice and the THE [31, 63, 22]. Overall the B20 compounds are as interesting as oxides and Heusler alloys, where one can tune spin-orbit effects, exchange parameters, and electronic structure by chemical engineering [76, 104]. This allows for precise control of the Berry phase properties in real and momentum space. Also the so-called mixed Berry curvature can be directly related to the DMI and the SOT by the torque-velocity correlation [49, 105].

The intrinsic AHE can be seen as the consequence of the momentum-space Berry curvature [103]. The AHE also has contributions from non-geometric extrinsic effects due to scattering off impurities and disorder giving rise to the side jump and the skew-scattering contributions (within the very oversimplified terminology). Correspondingly, the AHE, $\rho_{xy}^{\text{AHE}} = R_S M$, can

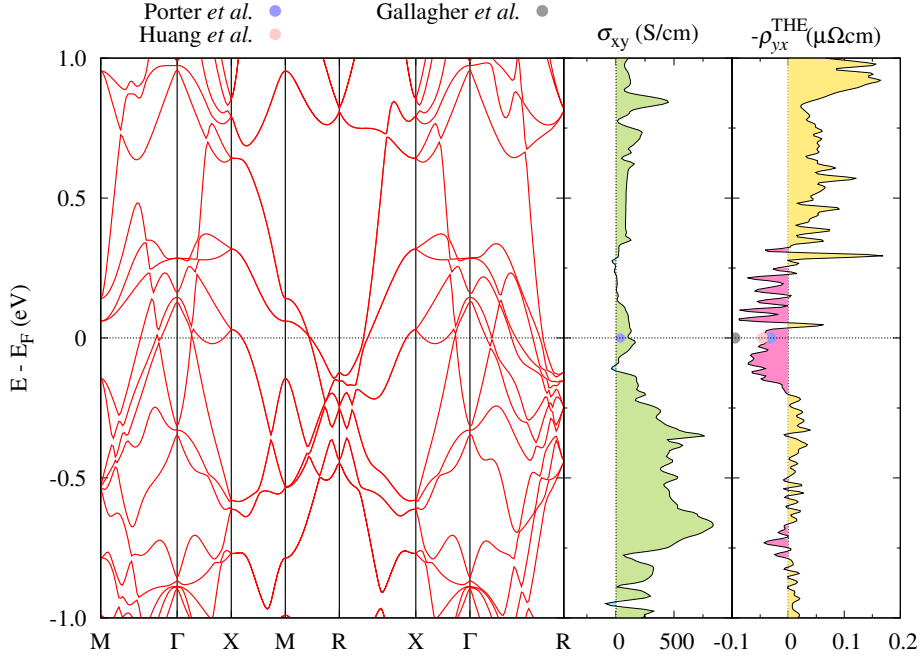


Figure 14: The band structure, anomalous Hall conductivity and topological Hall resistivity in FeGe as a function of the band filling, respectively. The values of ρ_{xy}^{THE} are compared with experimental results (dots) at the Fermi energy [22, 106, 23].

be separated into extrinsic and intrinsic mechanisms in terms of the longitudinal resistivity, $\rho_{xy}^{\text{AHE}} = [\alpha\rho_{xx} + (\beta + b)\rho_{xx}^2]M$, where α , β and b determine the contributions due to skew scattering, side-jump and intrinsic mechanisms, respectively [106]. In principle, it is often assumed that the strength and sign of the scattering mechanisms are strongly material and sample preparation dependent, whereas the intrinsic mechanism is purely dependent on the electronic structure of the clean crystal.

The intrinsic mechanism for the AHE (as well as the extrinsic ones) can be calculated from DFT using the Kubo linear response formalism [103]. In Fig. 13(b) and (c) the intrinsic AHE is plotted in MnFeSi [9] and MnFeGe [76] alloys, respectively. The size of the moment in the metallic MnFeSi compounds decreases with larger Fe concentration, where the moment is largest in MnSi ($\approx 0.4 \mu_B$) while FeSi is a nonmagnetic semiconducting compound. The calculated intrinsic AHE, obtained using the constrained LDA method, is in remarkable agreement with the experimental results shown in Figure 13(a). In comparison, the moments in MnFeGe range from 1.0–2.3 μ_B which is more than twice the values observed in MnFeSi. However, the intrinsic AHE is comparable in both alloys (see green curve in Fig. 13). Contrary to the smooth variation of the AHE in MnFeSi, the AHE in MnFeGe varies non-monotonically. This is due to the large variation of the Fermi surface and electronic structure in general in MnFeGe as a function of Fe concentration. In Fig. 14 we plot the band structure along with the AHE as a function of the band filling in FeGe which is compared with the experimental results [106]. The last panel shows the topological Hall resistivity which is discussed in the following [22, 106, 23].

Contrary to the AHE, which was discovered more than a century ago, the THE has only been observed and discussed within the last decade and a half. It makes sense to distinguish two limiting cases [107]: The contributions depend on the size of the magnetic texture, Λ_M , and the

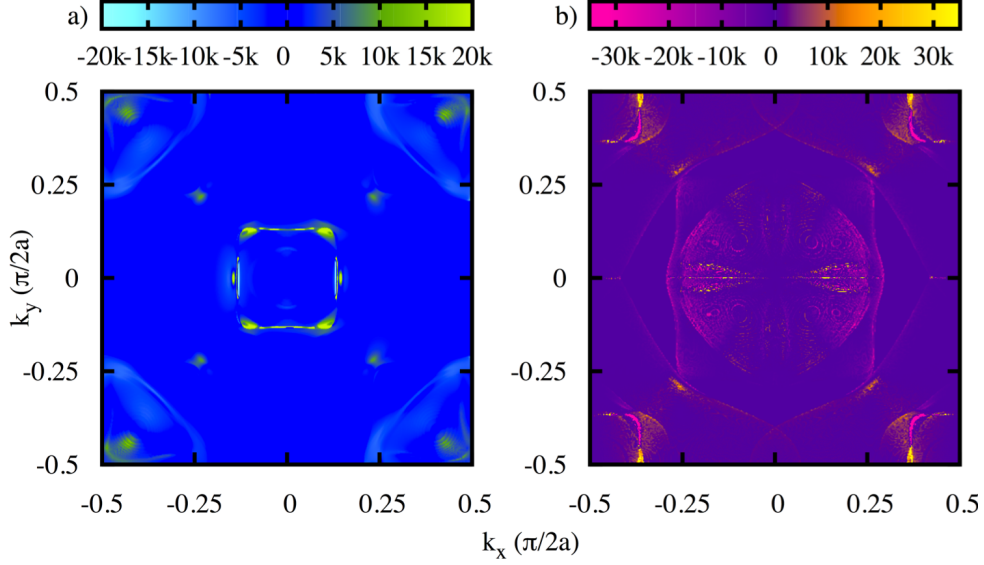


Figure 15: The momentum space contribution averaged over the \mathbf{k}_z direction to the Hall effects in FeGe at the Fermi energy: a) The momentum space dependent contribution to the Berry phase for the AHE. b) Momentum space contributions to the THE.

mean free path, l . In one case, where $l \gg \Lambda_M$, it can be evaluated directly from the electronic structure of the texture in reciprocal case. This “topological” contribution the Hall signal is often found in small scale skyrmions, hexagonal, and kagome discrete magnetic systems, and although it is not very clear neither how nor why to separate the THE from the AHE in this case, it is often argued that the THE originates in the finite spin chirality of the texture as given by $\Omega = \mathbf{S}_i \cdot (\mathbf{S}_j \times \mathbf{S}_k)$ [108], and might even exist without spin-orbit interaction. For a large scale of the texture, the scalar spin chirality transforms into the density of topological charge of the skyrmions. This brings us to the second mechanism for the THE in the regime when $l \ll \Lambda_M$. In this regime the adiabatic approximation is often applicable which justifies the application of the Berry phase effective framework for incorporating the effect of the smooth texture into the dynamical equations of electrons in terms of an emergent magnetic field, as discussed earlier [100, 101].

Within this second, adiabatic regime, the relation between the THE and the ordinary Hall effect (OHE) is analogous to the relation between the anomalous and the spin Hall effect, since the topological Hall conductivity can be obtained as the difference between the ordinary Hall conductivities for each spin and the OHE is obtained as their sum [9]. The corresponding semiclassical expression for the topological Hall conductivity reads:

$$\sigma_{xy}^{\text{THE},\sigma} \approx \sigma |B_{\text{eff}}^\sigma| \int \sum_n \tau_{\sigma n}^2 \left((v_{\mathbf{k}n}^x)^2 \cdot m_{\mathbf{k}n\sigma}^{yy} - v_{\mathbf{k}n}^x v_{\mathbf{k}n}^y \cdot m_{\mathbf{k}n\sigma}^{xy} \right) \frac{\partial f_0(\varepsilon_{\mathbf{k}n}^\sigma)}{\partial \varepsilon} \frac{d^3 k}{(2\pi)^3}, \quad (16)$$

where $m_{\mathbf{k}n\sigma}^{ij} = \frac{\partial^2 \varepsilon_{\mathbf{k}n}^\sigma}{\hbar^2 \partial k_i \partial k_j}$ is the inverse effective mass tensor, $\tau_{\sigma n}$ are the relaxation times, f_0 is the Fermi-Dirac distribution function, and $\varepsilon_{\mathbf{k}n}^\sigma$ are the eigenvalues. In practice it is easiest to calculate the topological Hall constant R_{xy}^{THE} by referring to the Boltzmann transport theory from above using the constant relaxation time approximation [9]. In this approximation we are able to calculate, from first principles, $R_{yx}^{\text{THE}} = \rho_{yx}^{\text{THE}}/B_{\text{eff}}$, which is parameter free. In turn, the topological Hall resistivity can be found as the difference in ordinary Hall conductivities for

each spin channel:

$$\rho_{yx}^{\text{THE}}(B_{\text{eff}}) = \frac{\sigma_{xy}^{\text{OHE},\uparrow}(B_{\text{eff}}) - \sigma_{xy}^{\text{OHE},\downarrow}(B_{\text{eff}})}{(\sigma_{xx}^{\uparrow} + \sigma_{xx}^{\downarrow})^2}. \quad (17)$$

In Fig. 13(c) and (d) the comparison of the experimental and calculated values of the topological Hall constant in MnFeSi is shown. For pure MnSi the value of about 3.0×10^{11} Ohm-m/T compares well to the experimental value of 4.5×10^{11} Ohm-m/T. Further, upon doping, both the experimental and theoretical variation of R^{THE} exhibit a change of sign and a noticeable reduction in magnitude in reasonable agreement with each other. This behavior can be understood on the basis of the band structure of paramagnetic MnSi in terms of (i) the change of sign of ordinary Hall conductivity for both spin channels, (ii) a significant decrease in magnitude of spin-up ordinary Hall conductivity as the Fe concentration increases, and (iii) a redistribution of the d states at the Fermi energy. In the last panel of Fig. 14 we plot the topological Hall resistivity as a function of the Fermi energy utilizing Eq. 17. To arrive at these values the magnitude of the effective field was calculated from $B_{\text{eff}} \approx 1/\Lambda_{\text{M}}^2$, where $\Lambda_{\text{M}} = 4\pi A/D$ was estimated based on first principle parameters for the exchange spin stiffness A and Dzyaloshinskii-Moriya interaction strength D . The extremely non-trivial behavior of the THE in FeGe as a function of energy explains the large variation of the topological Hall constant in magnitude for MnFeGe alloys, Fig. 13. In Fig. 15 we compare the momentum space distribution of the AHE and the topological Hall effect in FeGe (averaged over the \mathbf{k}_z -direction). In a) the Berry curvature of the AHE has distinct hot spots where interband transitions give rise to the AHE, whereas the momentum space contributions to the topological Hall effect are more dispersive due to the intraband nature of this phenomenon. The presented results thereby demonstrate the enormous sensitivity of the magnitude of the topological Hall signal to details of the electronic structure, in particular to the Fermi surface topology.

5.2 Topological spin Hall effect of antiferromagnetic skyrmions

In addition to previously considered ferromagnetic (FM) skyrmions it is worthwhile to estimate the transport properties of antiferromagnetic (AFM) skyrmions. To date, no true AFM skyrmions have been experimentally observed, possibly due to difficulties in detection of antiferromagnetic textures. With the advent of antiferromagnetic spintronics and the recent advances in controlling and detecting the antiferromagnetic domain walls, AFM skyrmions have naturally moved into research focus of the skyrmionics community.

Two distinct kinds of AFM skyrmions can be imagined: the synthetic AFM skyrmions [109], and the intrinsic AFM skyrmions [110, 111]. Similarly to the FM multilayer skyrmions considered in section 2.2, synthetic AFM skyrmions have AFM interlayer coupling thus keeping the skyrmionic texture within one layer and inverting the direction of local magnetization in the other (see Fig. 16d). The realization of intrinsic AFM skyrmions relies on in-plane nearest-neighbor AFM coupling so that the anti-parallel magnetic sublattices follow either a skyrmionic texture or its spin-reversed image [110, 111]. Since the winding number S (see Eq. 14) and the topological Hall effect change sign when inverting the magnetization direction, the combination of two skyrmion sublattices with opposite winding yields counter-propagating topological Hall currents. If the spin up and down states are degenerate, as it is the case for many AFMs, each spin sub-band

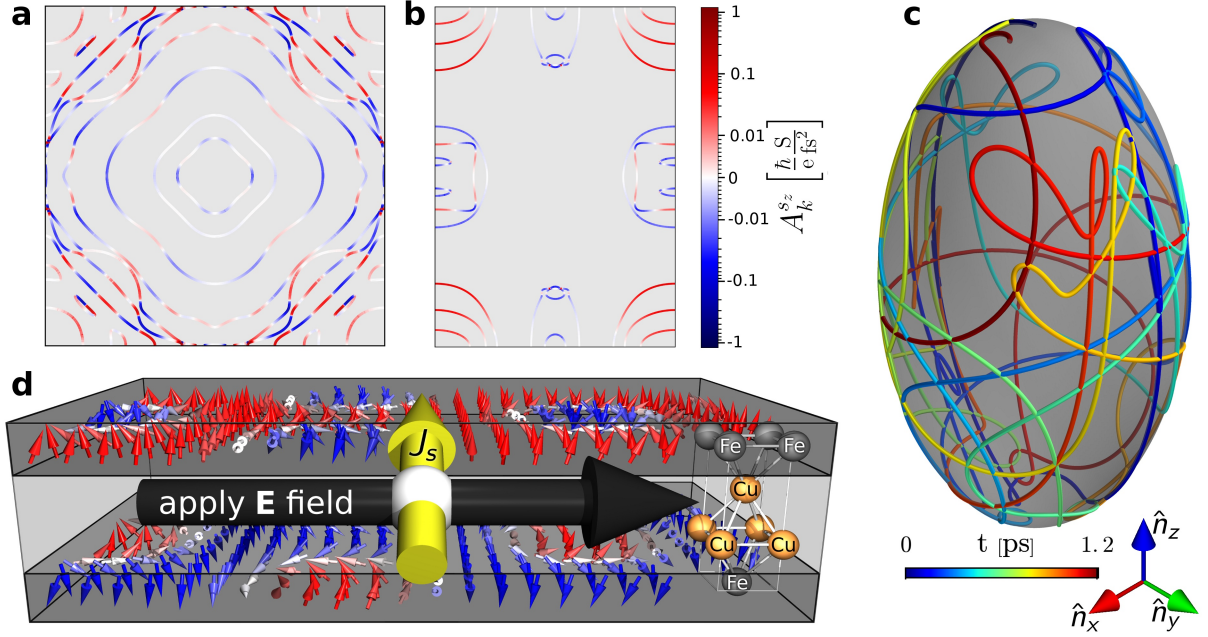


Figure 16: Fermi surface resolved contributions A_k^{sz} to the TSH conductivity for a) FeCu₆Fe trilayer and b) bcc Cr(110) thin film. c) Example spin trajectory in local frame restricted to a prolate spheroid with $\xi \approx 0.53$ for the case of a). d) Schematic picture of a FeCu_nFe trilayer system with imprinted synthetic AFM skyrmion lattice exhibiting the TSHE, where J_s stands for the transverse spin current generated by an applied electric field.

yields the same topological Hall constant with opposite sign. Hence, the topological Hall effect of *charge* in symmetric AFM skyrmions vanishes. On the contrary, the *spin* currents generated by each sublattice are added constructively which results in the so-called topological spin Hall effect (TSHE). In skyrmions of low-symmetry AFMs or ferrimagnets, for which the spin degeneracy of the bands does not occur, the charge cancellation is not enforced, so that the spin and charge topological Hall currents co-exist. In the following we restrict the discussion to the case of AFM skyrmions with spin-degenerate local band structure and vanishing charge THE, since they are most distinct in comparison to FM skyrmions.

Similar to their ferromagnetic counterpart several possibilities exist to calculate the topological spin Hall effect of AFM skyrmions. For small skyrmions it is possible to describe the whole skyrmion by considering large unit cells and diagonalizing the corresponding Hamiltonian [112]. Thereby the skyrmion's topology is effectively described in reciprocal space and the topological transport properties are encoded in the reciprocal Berry curvature, in analogy to the THE of small non-collinear structures mentioned before. Another prominent method for studying transport properties is the Landau-Büttiker approach in the Hall bar geometry, which can be also used to study the influence of skyrmion dynamics on transport [113]. In the following we describe a third possibility most applicable to large scale AFM skyrmion lattices [114].

The semiclassical approach has been already used in subsection 5.1 for FM skyrmions, however a significant modification of this method is necessary for AFM skyrmions. This method is based on tracking wave-packet trajectories as described by the semiclassical center-of-motion dynamics. While utilizing the semiclassical dynamics together with the Boltzmann equation in the FM case

yields Eq. 16, in the AFM case complications arise originated in the band's degenerate nature. The corresponding wave-packets are superpositions of spin up and down states with SU(2) gauge freedom, while the wave-packet's composition within the degenerate basis is described by the so-called isospin determining the wave-packet's relative spin character. The isospin has to be included into the coupled equations of motion [115] which further complicates finding their solution and enables the change of the wave-packet's spin throughout the evolution: a wave-packet initially aligned with the staggered order parameter can quickly become misaligned and even anti-aligned during the propagation in the texture (see Fig. 16c). This type of dynamics is governed by the overlap parameter $\xi(\mathbf{k})$ which reflects the strength of the coupling between two spin sublattices. According to the Boltzmann formalism in a thin film of thickness d_z the topological spin Hall conductivity reads

$$\sigma_{ij}^{\text{TSH}} = \tau^2 d_z \int d\mathbf{k} \frac{\partial f}{\partial E} (1 - \xi^2) \frac{\partial^2 \epsilon}{\partial k_j \partial k_l} [(\mathbf{s} \cdot \mathbf{n})(\dot{\mathbf{r}} \times \mathbf{B}_e)_l \dot{r}_i] \quad (18)$$

thus retaining the shape similar to that of FM skyrmions as given by Eq. 16. Additionally to the scaling by $(1 - \xi^2)$ factor, modifications arise due to the variation of the spin character of the wave-packets during the evolution and the emergent magnetic field's spin dependence via the $(\mathbf{s} \cdot \mathbf{n})$ term describing the spin alignment with the local staggered order parameter, \mathbf{n} . As a result, wave-packet's contributions to the TSHE can change tremendously during the evolution. Furthermore, the real-space velocity of the wave-packet, $\dot{\mathbf{r}}$, has a more complex structure owing to an additional anomalous velocity term originating in the systems non-abelian nature [114, 115]. Hence, $\dot{\mathbf{r}}$ becomes implicitly dependent on the spin alignment, which makes tracking of the precise evolution of the wave-packet in time necessary. Since the TSHE depends on the lifetime, an expedient quantity to look at is the topological spin Hall constant $R_{ji}^{\text{TSH}} = \sigma_{ij}^{\text{TSH}} / (\sigma_{ii} \sigma_{jj} B_{\text{eff}}^{\text{av}})$, which is independent of τ (in the constant relaxation time approximation), and, owing to the division by the averaged emergent magnetic field $B_{\text{eff}}^{\text{av}}$, depends little on the skyrmion size.

Starting from a collinear DFT calculation, one obtains the necessary reciprocal space properties in terms of the derivatives of the band energies and k -dependent overlaps of the states ξ . Additionally choosing a skyrmion lattice magnetic texture parameterization, all necessary parameters are available to estimate the TSHE. As a hypothetical example system for a synthetic AFM skyrmion, a Cu spacer sandwiched between two AFM coupled Fe monolayers with imprinted 3Q-skyrmionic lattice has been investigated, see Fig. 16(a,d) [114]. Overall, when translating spin to charge, the magnitude of the TSHE, as reflected in the topological spin Hall constant R^{TSH} , is found to be comparable to the FM version of the TSHE, i.e. the THE as given by R^{THE} and shown e.g. for MnSi in Fig. 13. Comparing to calculations which neglect the coupling ξ between the states localized on opposite spin sublattices, i.e. calculating the transport as if originating in two independent staggered FM systems, a significant enhancement of the signal is observed, while the qualitative trends, as for example the thickness dependence, remain comparable. As for intrinsic AFM skyrmions, taking as an example system a thin Cr(110) film, a similar magnitude of the TSHE values can be obtained, see Fig.16b. As the overlap ξ decreases the TSHE's magnitude \mathbf{k} -dependently and since \mathbf{k} -dependent conductivity contributions can compensate each other (see Fig.16(a,b)), huge variations, and even an increase of the TSHE could be also anticipated as compared to the uncoupled case [114]. Since both the THE and TSHE are Fermi surface properties, they are very sensitive to electronic structure details. Small

Fermi energy variations can cause large transport modifications, as shown for the THE in Fig.14. Especially crossing Dirac points and band edges has huge impact, which on the one hand offers a great engineering potential, while on the other makes *ab-initio* studies of the THE and TSHE computationally very demanding.

The *ab-initio* studies of the TSHE imply that the spin currents of typical magnitude found in calculations can be detected experimentally, resulting thus in an experimental observation of the AFM counterpart of the THE. Such a discovery would open new vistas for the detection of AFM skyrmions in various systems, and we believe that the TSHE will play the role similar to that of the conventional THE for the discovery of ferromagnetic skyrmions. Moreover, the prominent TSHE marks the AFM skyrmions as promising objects for pure spin current generation, which, as opposed to the spin Hall effect in paramagnets, is not relying on relativistic effects in the electronic structure. We suggest that such spin currents can be detected with standard techniques, i.e. by detecting the spin-torque that topological spin Hall currents would exert on a ferromagnet brought in contact with the AFM skyrmionic system, or by magneto-optical means in terms of corresponding spin accumulation at the edges of the sample.

Acknowledgments

Skyrmions and skyrmionics are central research topics of the institute Quantum Theory of Materials of PGI and IAS. We gratefully acknowledge the contributions of M. Hoffmann, B. Zimmermann and A. Nandy to this work. I.L.F. and S.L. thank D. M. Crum, J. Bouaziz and M. Bouhassoune for discussions and for the common work reviewed in section 4 (Single skyrmions from full first-principles). Work funded by the European Research Council (ERC) under the European Union's Horizon 2020 research and innovation programme (ERC-consolidator grant 681405 DYNASORE), the Brazilian funding agency CNPq under Project No. 233784/2014-4 and from the research and innovation programme under grant agreement number 665095 (FET-Open project MAGicSky).

References

- [1] A. Bogdanov and D. Yablonskii, Thermodynamically stable vortices in magnetically ordered crystals. The mixed state of magnets, *Zh. Eksp. Teor. Fiz* **95**(1), 178 (1989).
- [2] T. H. R. Skyrme, A unified field theory for mesons and baryons, *Nucl. Phys.* **31**, 556–569 (1962).
- [3] H.-B. Braun, Topological effects in nanomagnetism: from superparamagnetism to chiral quantum solitons, *Adv. Phys.* **61**, 1–116 (2012).
- [4] A. Fert, V. Cros, and J. Sampaio, Skyrmions on the track, *Nature Nanotech.* **8**(3), 152–156 (2013).
- [5] I. E. Dzialoshinskii, Thermodynamic Theory of "Weak" Ferromagnetism In Antiferromagnetic Substances, *Sov. Phys. JETP* **5**, 1259 (1957).

- [6] T. Moriya, Anisotropic Superexchange Interaction and Weak Ferromagnetism, *Phys. Rev.* **120**, 91–98 (1960).
- [7] M. dos Santos Dias, J. Bouaziz, M. Bouhassoune, S. Blügel, and S. Lounis, Chirality-driven orbital magnetic moments as a new probe for topological magnetic structures, *Nature Commun.* **7**, 13613 (2016).
- [8] T. Schulz, R. Ritz, A. Bauer, M. Halder, M. Wagner, C. Franz, C. Pfleiderer, K. Everschor, M. Garst, and A. Rosch, Emergent electrodynamics of skyrmions in a chiral magnet, *Nature Phys.* **8**(4), 301–304 (2012).
- [9] C. Franz, F. Freimuth, A. Bauer, R. Ritz, C. Schnarr, C. Duvinage, T. Adams, S. Blügel, A. Rosch, Y. Mokrousov, and C. Pfleiderer, Real-Space and Reciprocal-Space Berry Phases in the Hall Effect of $\text{Mn}_{1-x}\text{Fe}_x\text{Si}$, *Phys. Rev. Lett.* **112**, 186601 (2014).
- [10] D. M. Crum, M. Bouhassoune, J. Bouaziz, B. Schweffinghaus, S. Blügel, and S. Lounis, Perpendicular reading of single confined magnetic skyrmions, *Nature Commun.* **6**, 8541 (2015).
- [11] C. Hanneken, F. Otte, A. Kubetzka, B. Dupé, N. Romming, K. von Bergmann, R. Wiesendanger, and S. Heinze, Electrical detection of magnetic skyrmions by tunnelling non-collinear magnetoresistance, *Nature Nanotech.* **10**, 1039 (2015).
- [12] S. Woo, K. Litzius, B. Kruger, Y. M. Im, L. Caretta, K. Richter, M. Mann, A. Krone, R. M. Reeve, M. Weigand, P. Agrawal, I. Lemesh, M. A. Mawass, P. Fischer, M. Kläui, and B. G. S, Observation of room-temperature magnetic skyrmions and their current-driven dynamics in ultrathin metallic ferromagnets, *Nature Materials* **15**, 501 (2016).
- [13] J. Sampaio, V. Cros, S. Rohart, A. Thiaville, and A. Fert, Nucleation, stability and current-induced motion of isolated magnetic skyrmions in nanostructures, *Nature Nanotech.* **8**, 839844 (2013).
- [14] X. Yu, D. Morikawa, Y. Tokunaga, M. Kubota, T. Kurumaji, H. Oike, M. Nakamura, F. Kagawa, Y. Taguchi, T. Arima, M. Kawasaki, and Y. Tokura, Current-Induced Nucleation and Annihilation of Magnetic Skyrmions at Room Temperature in a Chiral Magnet, *Adv. Mater.* **29**, 1606178 (2017).
- [15] S. Mühlbauer, B. Binz, F. Jonietz, C. Pfleiderer, A. Rosch, A. Neubauer, R. Georgii, and P. Böni, Skyrmion lattice in a chiral magnet, *Science* **323**(5916), 915–919 (2009).
- [16] H. Wilhelm, M. Baenitz, M. Schmidt, U. Rößler, A. Leonov, and A. Bogdanov, Precursor phenomena at the magnetic ordering of the cubic helimagnet FeGe, *Phys. Rev. Lett.* **107**(12), 127203 (2011).
- [17] X. Yu, Y. Onose, N. Kanazawa, J. Park, J. Han, Y. Matsui, N. Nagaosa, and Y. Tokura, Real-space observation of a two-dimensional skyrmion crystal, *Nature* **465**(7300), 901–904 (2010).

- [18] H. Du, R. Che, L. Kong, X. Zhao, C. Jin, C. Wang, J. Yang, W. Ning, R. Li, C. Jin, et al., Edge-mediated skyrmion chain and its collective dynamics in a confined geometry, *Nature Commun.* **6**, 8504 (2015).
- [19] A. Tonomura, X. Yu, K. Yanagisawa, T. Matsuda, Y. Onose, N. Kanazawa, H. S. Park, and Y. Tokura, Real-space observation of skyrmion lattice in helimagnet MnSi thin samples, *Nano Lett.* **12**, 1673 (2012).
- [20] S. Meynell, M. Wilson, H. Fritzsche, A. Bogdanov, and T. Monchesky, Surface twist instabilities and skyrmion states in chiral ferromagnets, *Phys. Rev. B* **90**(1), 014406 (2014).
- [21] M. Wilson, A. Butenko, A. Bogdanov, and T. Monchesky, Chiral skyrmions in cubic helimagnet films: The role of uniaxial anisotropy, *Phys. Rev. B* **89**(9), 094411 (2014).
- [22] S. X. Huang and C. L. Chien, Extended Skyrmion Phase in Epitaxial FeGe(111) Thin Films, *Phys. Rev. Lett.* **108**, 267201 (2012).
- [23] J. C. Gallagher, K. Y. Meng, J. T. Brangham, H. L. Wang, B. D. Esser, D. W. McComb, and F. Y. Yang, Robust Zero-Field Skyrmion Formation in FeGe Epitaxial Thin Films, *Physical Review Letters* **118**(2), 027201 (2017).
- [24] N. Kiselev, A. Bogdanov, R. Schäfer, and U. Rößler, Chiral skyrmions in thin magnetic films: new objects for magnetic storage technologies?, *J. Phys. D: Appl. Phys.* **44**(39), 392001 (2011).
- [25] N. Nagaosa and Y. Tokura, Topological properties and dynamics of magnetic skyrmions, *Nature Nanotech.* **8**, 899 (2013).
- [26] N. Romming, C. Hanneken, M. Menzel, J. E. Bickel, B. Wolter, K. von Bergmann, A. Kubetzka, and R. Wiesendanger, Writing and Deleting Single Magnetic Skyrmions, *Science* **341**, 636 (2013).
- [27] B. Dupé, G. Bihlmayer, M. Böttcher, S. Blügel, and S. Heinze, Engineering skyrmions in transition-metal multilayers for spintronics, *Nature Comms.* **7**, 11779 (2016).
- [28] X. Yu, N. Kanazawa, W. Zhang, T. Nagai, T. Hara, K. Kimoto, Y. Matsui, Y. Onose, and Y. Tokura, Skyrmion flow near room temperature in an ultralow current density, *Nature Comms.* **3**, 988 (2012).
- [29] F. Jonietz, S. Mühlbauer, C. Pfleiderer, A. Neubauer, W. Münzer, A. Bauer, T. Adams, R. Georgii, P. Böni, R. A. Duine, K. Everschor, M. Garst, and A. Rosch, Spin Transfer Torques in MnSi at Ultralow Current Densities, *Science* **330**(6011), 1648–1651 (2010).
- [30] F. Freimuth, R. Bamler, Y. Mokrousov, and A. Rosch, Phase-space Berry phases in chiral magnets: Dzyaloshinskii-Moriya interaction and the charge of skyrmions, *Phys. Rev. B* **88**, 214409 (2013).
- [31] A. Neubauer, C. Pfleiderer, B. Binz, A. Rosch, R. Ritz, P. G. Niklowitz, and P. Böni, Topological Hall Effect in the A Phase of MnSi, *Phys. Rev. Lett.* **102**, 186602 (2009).

- [32] W. P. Pratt, S.-F. Lee, J. M. Slaughter, R. Loloee, P. A. Schroeder, and J. Bass, Perpendicular giant magnetoresistances of Ag/Co multilayers, *Phys. Rev. Lett.* **66**, 3060–3063 (1991).
- [33] B. Zimmermann, M. Heide, G. Bihlmayer, and S. Blügel, First-principles analysis of a homo-chiral cycloidal magnetic structure in a monolayer Cr on W(110), *Phys. Rev. B* **90**, 115427 (2014).
- [34] B. Schweflinghaus, B. Zimmermann, M. Heide, G. Bihlmayer, and S. Blügel, Role of Dzyaloshinskii-Moriya interaction for magnetism in transition-metal chains at Pt step-edges, *Phys. Rev. B* **94**, 024403 (2016).
- [35] F. Freimuth, Y. Mokrousov, D. Wortmann, S. Heinze, and S. Blügel, Maximally localized Wannier functions within the FLAPW formalism, *Phys. Rev. B* **78**, 035120 (Jul 2008).
- [36] C. Herring, *Exchange interactions among itinerant electrons, Magnetism Vol. IV*, ed. G. T. Rado, H. Suhl, Academic Press, New York, London, 1966.
- [37] L. M. Sandratskii, Symmetry analysis of electronic states for crystals with spiral magnetic order. I. General properties, *J. Phys.: Condens. Matter* **3**, 8565 (1991).
- [38] E. Wimmer, H. Krakauer, M. Weinert, and A. J. Freeman, Full-potential self-consistent linearized-augmented-plane-wave method for calculating the electronic structure of molecules and surfaces: O₂ molecule, *Phys. Rev. B* **24**, 864 (1981).
- [39] P. Kurz, F. Förster, L. Nordström, G. Bihlmayer, and S. Blügel, *Ab initio* treatment of non-collinear magnets with the full-potential linearized augmented planewave method, *Phys. Rev. B* **69**, 024415 (2004).
- [40] T. A. Kaplan, Frustrated classical Heisenberg model in one dimension with nearest-neighbor biquadratic exchange: Exact solution for the ground-state phase diagram, *Phys. Rev. B* **80**, 012407 (2009).
- [41] P. Kurz, G. Bihlmayer, K. Hirai, and S. Blügel, Three-Dimensional Spin-Structure on a Two-Dimensional Lattice: Mn/Cu(111), *Phys. Rev. Lett.* **86**, 1106 (2001).
- [42] V. P. Antropov, M. I. Katsnelson, M. van Schilfhaarde, and B. N. Harmon, *AbInitio* Spin Dynamics in Magnets, *Phys. Rev. Lett.* **75**, 729–732 (1995).
- [43] V. P. Antropov, M. I. Katsnelson, B. N. Harmon, M. van Schilfhaarde, and D. Kusnezov, Spin dynamics in magnets: Equation of motion and finite temperature effects, *Phys. Rev. B* **54**, 1019–1035 (1996).
- [44] B. Hardrat, A. Al-Zubi, P. Ferriani, S. Blügel, G. Bihlmayer, and S. Heinze, Complex magnetism of Fe monolayers on hexagonal transition-metal surfaces from first principles, *Phys. Rev. B* **79**, 094411 (2009).
- [45] M. Ležaić, P. Mavropoulos, G. Bihlmayer, and S. Blügel, Exchange interactions and local-moment fluctuation corrections in ferromagnets at finite temperatures based on non-collinear density-functional calculations, *Phys. Rev. B* **88**, 134403 (2013).

- [46] D. A. Smith, New mechanisms for magnetic anisotropy in localised s-state moment materials, *J. Magn. Magn. Mater.* **1**, 214 (1976).
- [47] M. Heide, G. Bihlmayer, and S. Blügel, Describing Dzyaloshinskii-Moriya spirals from first principles, *Physica B* **404**, 2678 (2009).
- [48] L. Udvardi, L. Szunyogh, K. Palotás, and P. Weinberger, First-principles relativistic study of spin waves in thin magnetic films, *Phys. Rev. B* **68**, 104436 (2003).
- [49] F. Freimuth, S. Blügel, and Y. Mokrousov, Berry phase theory of Dzyaloshinskii-Moriya interaction and spin-orbit torques, *Journal of Physics: Condensed Matter* **26**, 104202 (2014).
- [50] K. von Bergmann, S. Heinze, M. Bode, E. Y. Vedmedenko, G. Bihlmayer, S. Blügel, and R. Wiesendanger, Observation of a complex nanoscale magnetic structure in a hexagonal Fe monolayer, *Phys. Rev. Lett.* **96**, 167203 (2006).
- [51] K. von Bergmann, S. Heinze, M. Bode, G. Bihlmayer, S. Blügel, and R. Wiesendanger, Complex magnetism of the Fe monolayer on Ir(111), *New J. Phys.* **9**, 396 (2007).
- [52] S. Heinze, P. Kurz, D. Wortmann, G. Bihlmayer, and S. Blügel, Complex magnetism in ultra-thin films: atomic-scale spin structures and resolution by the spin-polarized scanning tunneling microscope, *Appl. Phys. A* **75**, 25 (2002).
- [53] S. Heinze, K. von Bergmann, M. Menzel, J. Brede, A. Kubetzka, R. Wiesendanger, G. Bihlmayer, and S. Blügel, Spontaneous atomic-scale magnetic skyrmion lattice in two dimensions, *Nature Phys.* **7**, 713 (2011).
- [54] M. Bode, M. Heide, K. v. Bergmann, P. Ferriani, S. Heinze, G. Bihlmayer, A. Kubetzka, O. Pietzsch, S. Blügel, and R. Wiesendanger, Chiral magnetic order at surfaces driven by inversion asymmetry, *Nature* **447**, 190 (2007).
- [55] M. Hoffmann, B. Zimmermann, G. P. Müller, D. Schürhoff, N. S. Kiselev, C. Melcher, and S. Blügel, Antiskyrmions stabilized at interfaces by anisotropic Dzyaloshinskii-Moriya interactions, *Nature Comms.* **8**, 308 (2017).
- [56] K. von Bergmann, M. Menzel, A. Kubetzka, and R. Wiesendanger, Influence of the Local Atom Configuration on a Hexagonal Skyrmion Lattice, *Nano Letters* **15**, 3280 (2015).
- [57] M. D. Santis, Y. Gauthier, H. C. N. Tolentino, G. Bihlmayer, S. Blügel, and V. Langlais, Structure and magnetic properties of Mn/Pt(110)-(1x2): a joint x-ray diffraction and theoretical study, *Phys. Rev. B* **75**, 205432 (2007).
- [58] S. Di Napoli, A. M. Llois, G. Bihlmayer, S. Blügel, M. Alouani, and H. Dreyssé, Magnetic structure and transport properties of noncollinear LaMn_2X_2 ($X = \text{Ge}, \text{Si}$) systems, *Phys. Rev. B* **70**, 174418 (2004).
- [59] B. Dupé, M. Hoffmann, C. Paillard, and S. Heinze, Tailoring magnetic skyrmions in ultra-thin transition metal films, *Nature Commun.* **5**, 4030 (2014).

- [60] L. Rózsa, E. Simon, K. Palotás, L. Udvardi, and L. Szunyogh, Complex magnetic phase diagram and skyrmion lifetime in an ultrathin film from atomistic simulations, *Phys. Rev. B* **93**, 024417 (Jan 2016).
- [61] A. Belabbes, G. Bihlmayer, F. Bechstedt, S. Blügel, and A. Manchon, Hund’s rule-driven Dzyaloshinskii-Moriya interaction at $3d$ - $5d$ interfaces, *Phys. Rev. Lett.* **117**, 247202 (2016).
- [62] X. Yu, A. Kikkawa, D. Morikawa, K. Shibata, Y. Tokunaga, Y. Taguchi, and Y. Tokura, Variation of skyrmion forms and their stability in MnSi thin plates, *Phys. Rev. B* **91**, 054411 (2015).
- [63] X. Yu, N. Kanazawa, Y. Onose, K. Kimoto, W. Zhang, S. Ishiwata, Y. Matsui, and Y. Tokura, Near room-temperature formation of a skyrmion crystal in thin-films of the helimagnet FeGe, *Nature Mater.* **10**(2), 106–109 (2011).
- [64] K. Shibata, X. Yu, T. Hara, D. Morikawa, N. Kanazawa, K. Kimoto, S. Ishiwata, Y. Matsui, and Y. Tokura, Towards control of the size and helicity of skyrmions in helimagnetic alloys by spin-orbit coupling, *Nature Nanotech.* **8**(10), 723–728 (2013).
- [65] T. Yokouchi, N. Kanazawa, A. Tsukazaki, Y. Kozuka, M. Kawasaki, M. Ichikawa, F. Kagawa, and Y. Tokura, Stability of two-dimensional skyrmions in thin films of $\text{Mn}_{1-x}\text{Fe}_x\text{Si}$ investigated by the topological Hall effect, *Phys. Rev. B* **89**(6), 064416 (2014).
- [66] I. Dzyaloshinskii, Theory of helicoidal structures in antiferromagnets. III, *Sov. Phys. JETP-USSR* **20**(3), 665 (1965).
- [67] B. Lebech, J. Bernhard, and T. Freltoft, Magnetic structures of cubic FeGe studied by small-angle neutron scattering, *J. Phys. Condens. Matter* **1**(35), 6105 (1989).
- [68] S. Maleyev, A-phase origin in B20 helimagnets, arXiv preprint arXiv:1102.3524 (2011).
- [69] A. Leonov, U. Röfler, and A. Bogdanov, Phenomenological theory of magnetization reversal in nanosystems with competing anisotropies, *J. Appl. Phys.* **104**(8), 084304 (2008).
- [70] A. Bogdanov and A. Hubert, Thermodynamically stable magnetic vortex states in magnetic crystals, *JMMM* **138**(3), 255–269 (1994).
- [71] F. N. Rybakov, A. B. Borisov, S. Blügel, and N. S. Kiselev, New Type of Stable Particlelike States in Chiral Magnets, *Phys. Rev. Lett.* **115**, 117201 (2015).
- [72] F. Rybakov, A. Borisov, and A. Bogdanov, Three-dimensional skyrmion states in thin films of cubic helimagnets, *Phys. Rev. B* **87**(9), 094424 (2013).
- [73] V. Baryakhtar and E. Stefanovsky, Spin wave spectrum in antiferromagnets having a spiral magnetic structure, *Sov. Phys. Solid State* **11**(7), 1566 (1970).
- [74] P. Bak and M. H. Jensen, Theory of helical magnetic structures and phase transitions in MnSi and FeGe, *J. Phys. C: Solid State Phys.* **13**(31), L881 (1980).

- [75] T. Koretsune, N. Nagaosa, and R. Arita, Control of Dzyaloshinskii-Moriya interaction in $\text{Mn}_{1-x}\text{Fe}_x\text{Ge}$: a first-principles study, *Scientific Rep.* **5**, 13302 (2015).
- [76] J. Gayles, F. Freimuth, T. Schena, G. Lani, P. Mavropoulos, R. Duine, S. Blügel, J. Sinova, and Y. Mokrousov, Dzyaloshinskii-Moriya interaction and Hall effects in the skyrmion phase of $\text{Mn}_{1-x}\text{Fe}_x\text{Ge}$, *Phys. Rev. Lett.* **115**(3), 036602 (2015).
- [77] T. Kikuchi, T. Koretsune, R. Arita, and G. Tatara, Dzyaloshinskii-Moriya interaction as a consequence of a Doppler shift due to spin-orbit-induced intrinsic spin current, *Phys. Rev. Lett.* **116**(24), 247201 (2016).
- [78] S. Do Yi, S. Onoda, N. Nagaosa, and J. H. Han, Skyrmions and anomalous Hall effect in a Dzyaloshinskii-Moriya spiral magnet, *Phys. Rev. B* **80**(5), 054416 (2009).
- [79] V. A. Chizhikov and V. E. Dmitrienko, Frustrated magnetic helices in MnSi-type crystals, *Phys. Rev. B* **85**(1), 014421 (2012).
- [80] V. A. Chizhikov and V. E. Dmitrienko, Multishell contribution to the Dzyaloshinskii-Moriya spiraling in MnSi-type crystals, *Phys. Rev. B* **88**(21), 214402 (2013).
- [81] F. N. Rybakov, A. B. Borisov, S. Blügel, and N. S. Kiselev, New spiral state and skyrmion lattice in 3D model of chiral magnets, *New J. Phys.* **18**(4), 045002 (2016).
- [82] D. Weller and A. Moser, Thermal effect limits in ultrahigh-density magnetic recording, *IEEE Trans. Mag.* **35**(6), 4423–4439 (1999).
- [83] S. Parkin and S.-H. Yang, Memory on the racetrack, *Nature Nanotech.* **10**(3), 195–198 (2015).
- [84] J. Müller, Magnetic skyrmions on a two-lane racetrack, *New J. Phys.* **19**(2), 025002 (2017).
- [85] F. Zheng, N. Rybakov, Philipp, B. Borisov, Aleksandr, D. Song, S. Wang, Z.-A. Li, H. Du, N. S. Kiselev, J. Caron, A. Kovács, M. Tian, Y. Zhang, S. Blügel, and E. Dunin-Borkowski, Rafal, Experimental observation of magnetic bobbbers for a new concept of magnetic solid-state memory, arXiv:1706.04654 (2017).
- [86] M. dos Santos Dias and S. Lounis, Insights into the orbital magnetism of noncollinear magnetic systems, *SPIE* **10357**, 103572A (2017).
- [87] D. Bauer, Development of a relativistic full-potential first-principles multiple scattering Green function method applied to complex magnetic textures of nano structures at surfaces, Ph.D. thesis, RWTH Aachen University (2014).
- [88] N. Romming, A. Kubetzka, C. Hanneken, K. von Bergmann, and R. Wiesendanger, Field-Dependent Size and Shape of Single Magnetic Skyrmions, *Phys. Rev. Lett.* **114**, 177203 (2015).
- [89] A. Kubetzka, C. Hanneken, R. Wiesendanger, and K. von Bergmann, Impact of the skyrmion spin texture on magnetoresistance, *Phys. Rev. B* **95**, 104433 (2017).

- [90] L. Rózsa, A. Deák, E. Simon, R. Yanes, L. Udvardi, L. Szunyogh, and U. Nowak, Skyrmions with Attractive Interactions in an Ultrathin Magnetic Film, *Phys. Rev. Lett.* **117**, 157205 (Oct 2016).
- [91] L. Rózsa, K. Palotás, A. Deák, E. Simon, R. Yanes, L. Udvardi, L. Szunyogh, and U. Nowak, Formation and stability of metastable skyrmionic spin structures with various topologies in an ultrathin film, *Phys. Rev. B* **95**, 094423 (Mar 2017).
- [92] A. K. Nandy, N. S. Kiselev, and S. Blügel, Interlayer Exchange Coupling: A General Scheme Turning Chiral Magnets into Magnetic Multilayers Carrying Atomic-Scale Skyrmions, *Phys. Rev. Lett.* **116**, 177202 (Apr 2016).
- [93] P.-J. H. Hsu, A. Finco, N. Romming, K. von Bergmann, and R. Wiesendanger, Electric-field-driven switching of individual magnetic skyrmions, *Nature Nanotech.* **12**, 123 (2017).
- [94] S. Alexander and P. W. Anderson, Interaction Between Localized States in Metals, *Phys. Rev.* **133**, A1594–A1603 (1964).
- [95] A. Oswald, R. Zeller, P. J. Braspenning, and P. H. Dederichs, Interaction of magnetic impurities in Cu and Ag, *Journal of Physics F: Metal Physics* **15**(1), 193 (1985).
- [96] N. Kanazawa, M. Kubota, A. Tsukazaki, Y. Kozuka, K. S. Takahashi, M. Kawasaki, M. Ichikawa, F. Kagawa, and Y. Tokura, Discretized topological Hall effect emerging from skyrmions in constricted geometry, *Phys. Rev. B* **91**, 041122 (2015).
- [97] S. Zhang and P. M. Levy, Conductivity perpendicular to the plane of multilayered structures, *Journal of Applied Physics* **69**(8), 4786–4788 (1991).
- [98] J. Tersoff and D. R. Hamann, Theory and Application for the Scanning Tunneling Microscope, *Phys. Rev. Lett.* **50**, 1998–2001 (1983).
- [99] I. L. Fernandes, J. Bouaziz, M. Bouhassoune, S. Blügel, and S. Lounis, Universality of defect-skyrmion interaction profiles, submitted to *Nature Commun.* (2018).
- [100] P. Bruno, V. K. Dugaev, and M. Taillefumier, Topological Hall Effect and Berry Phase in Magnetic Nanostructures, *Physical Review Letters* **93**(9), 96806 (2004).
- [101] G. Metalidis and P. Bruno, Topological Hall effect studied in simple models, *Physical Review B* **74**(4), 045327 (2006).
- [102] R. Ritz, M. Halder, C. Franz, A. Bauer, M. Wagner, R. Bamler, A. Rosch, and C. Pfleiderer, Giant generic topological Hall resistivity of MnSi under pressure, *Physical Review B* **87**(13), 134424 (2013).
- [103] N. Nagaosa, J. Sinova, S. Onoda, A. H. MacDonald, and N. P. Ong, Anomalous Hall effect, *Reviews of Modern Physics* **82**(2), 1539–1592 (2010).
- [104] N. Kanazawa, Y. Onose, T. Arima, D. Okuyama, K. Ohoyama, S. Wakimoto, K. Kakurai, S. Ishiwata, and Y. Tokura, Large Topological Hall Effect in a Short-Period Helimagnet MnGe, *Phys. Rev. Lett.* **106**(15), 156603 (2011).

- [105] F. Freimuth, S. Blügel, and Y. Mokrousov, Relation of the Dzyaloshinskii-Moriya interaction to spin currents and to the spin-orbit field, *Physical Review B* **96**(5), 054403 (2017).
- [106] N. A. Porter, J. C. Gartside, and C. H. Marrows, Scattering mechanisms in textured FeGe thin films: magnetoresistance and the anomalous Hall effect, *Arxiv Preprint arxiv:1402.1402.1276* (2014).
- [107] Y. Shiomi, S. Iguchi, and Y. Tokura, Emergence of topological Hall effect from fanlike spin structure as modified by Dzyaloshinsky-Moriya interaction in MnP, *Physical Review B* **86**(18), 180404 (2012).
- [108] C. Sürgers, G. Fischer, P. Winkel, and H. V. Löhneysen, Large topological Hall effect in the non-collinear phase of an antiferromagnet., *Nat. Commun.* **5**, 3400 (2014).
- [109] X. Zhang, Y. Zhou, and M. Ezawa, Magnetic bilayer-skyrmions without skyrmion Hall effect., *Nat. Commun.* **7**, 10293 (2016).
- [110] X. Zhang, Y. Zhou, and M. Ezawa, Antiferromagnetic Skyrmion: Stability, Creation and Manipulation, *Sci. Rep.* **6**, 24795 (2016).
- [111] J. Barker and O. A. Tretiakov, Static and Dynamical Properties of Antiferromagnetic Skyrmions in the Presence of Applied Current and Temperature, *Phys. Rev. Lett.* **116**(14), 147203 (2016).
- [112] B. Göbel, A. Mook, J. Henk, and I. Mertig, Antiferromagnetic skyrmion crystals: Generation, topological Hall, and topological spin Hall effect, *Phys. Rev. B* **96**(6), 060406 (2017).
- [113] C. A. Akosa, O. A. Tretiakov, G. Tatara, and A. Manchon, Theory of Topological Spin Hall Effect in Antiferromagnetic Skyrmion: Impact on Current-induced Motion, *arXiv* , 1709.02931 (2017).
- [114] P. M. Buhl, F. Freimuth, S. Blügel, and Y. Mokrousov, Topological spin Hall effect in antiferromagnetic skyrmions, *Phys. status solidi - Rapid Res. Lett.* **11**(4), 1700007 (2017).
- [115] R. Cheng and Q. Niu, Electron dynamics in slowly varying antiferromagnetic texture, *Phys. Rev. B* **86**(24), 245118 (2012).